Atmospheric
Chemistry
and Physics
Discussions

Impact of the Variability in Vertical Separation between Biomass-Burning Aerosols and Marine Stratocumulus on Cloud Microphysical Properties over the Southeast Atlantic

Siddhant Gupta[1,2], Greg M. McFarquhar[1,2], Joseph R. O'Brien[3], David J. Delene[3], Michael R. Poellot[3], Amie Dobracki[4], James R. Podolske[5], Jens Redemann[2], Samuel E. LeBlanc[5,6], Michal Segal-Rozenhaimer[5,6,7] and Kristina Pistone[5,6]

[1]Cooperative Institute for Mesoscale Meteorological Studies, University of Oklahoma, Norman, OK, USA
[2]School of Meteorology, University of Oklahoma, Norman, OK, USA
[3]Department of Atmospheric Sciences, University of North Dakota, Grand Forks, ND, USA
[4]Department of Atmospheric Sciences, Rosenstiel School of Marine and Atmospheric Science, University of Miami, Miami, FL, USA
[5]NASA Ames Research Center, Moffett Field, CA, USA
[6]Bay Area Environmental Research Institute, Moffett Field, CA, USA
[7]Department of Geophysics and Planetary Sciences, Porter School of Environmental and Earth Sciences, Tel Aviv University, Tel Aviv, Israel

Correspondence to: Siddhant Gupta (sid@ou.edu)

Abstract. Marine stratocumulus cloud properties over the southeast Atlantic Ocean are impacted by contact between above-cloud biomass-burning aerosols and cloud tops. Different vertical separations (0 to 2000 m) between the aerosol layer and cloud tops were observed on six research flights in September 2016 during the NASA ObseRvations of Aerosols above CLouds and their intEractionS (ORACLES) field campaign. There were 30 *contact* profiles where the aerosol layer with aerosol concentration (N_a) > 500 cm^{-3} was within 100 m of cloud tops, and 41 *separated* profiles where the aerosol layer with N_a > 500 cm^{-3} was located more than 100 m above cloud tops. For *contact* profiles, the average cloud droplet concentration (N_c) in the cloud layer was up to 68 cm^{-3} higher, the effective radius (R_e) up to 1.3 µm lower and the liquid water content (LWC) within 0.01 g m^{-3} compared to *separated* profiles. Free tropospheric humidity was higher in the presence of biomass-burning aerosols and *contact* profiles had a smaller decrease in humidity (and positive buoyancy) across cloud tops due to higher median above-cloud N_a (895 cm^{-3}) compared to *separated* profiles (30 cm^{-3}). Due to droplet evaporation from entrainment mixing of warm, dry free tropospheric air into the clouds, the median N_c and LWC for *contact* profiles decreased with height by 21% and 9% in the top 20% of the cloud layer. The impact of droplet evaporation was stronger during *separated* profiles as a greater decrease in humidity (and negative buoyancy) across cloud tops led to greater decreases in median N_c (30%) and LWC (16%) near cloud tops.

Below-cloud N_a was sampled during 61 profiles, and most *contact* profiles (20 out of 28) were within high-N_a (> 350 cm^{-3}) boundary layers while most *separated* profiles (22 out of 33) were within low-N_a (< 350 cm^{-3}) boundary layers. Although, the differences in below-cloud N_a were statistically insignificant, *contact* profiles within low-N_a boundary layers had up to 34.9 cm^{-3} higher N_c compared to *separated* profiles. This was driven by the weaker impact of droplet evaporation

35   in the presence of biomass-burning aerosols within 100 m above cloud tops. For *contact* profiles within high-N_a boundary layers, the presence of biomass-burning aerosols led to higher below-cloud N_a (up to 70.5 cm^{-3}) and additional droplet nucleation above cloud base along with weaker droplet evaporation. Consequently, the *contact* profiles in high-N_a boundary layers had up to 88.4 cm^{-3} higher N_c compared to *separated* profiles. These results motivate investigations of aerosol-cloud-precipitation interactions over the southeast Atlantic since the changes in N_c, R_e, and LWC induced by the presence of

40   above-cloud biomass burning aerosols are likely to impact precipitation rates, liquid water path and cloud fraction, and modulate closed to open cell transitions.

1 Introduction

Globally averaged annual cloud cover can reach up to 61% of the Earth's surface (Warren et al., 1988) and contributes a radiative forcing of about -22 W m^{-2} to Earth's energy budget (Hartmann et al., 1992). In comparison, the estimated radiative

45   forcing from 1750 to 2011 due to well-mixed greenhouse gases is +2.83 W m^{-2} (Myhre et al., 2013). Cloud radiative effects (CREs) include reflection of shortwave solar radiation to space, which cools the Earth, and the absorption (emission) of longwave radiation which warms (cools) the Earth. Marine stratocumulus is a common cloud type that is observed over oceans off western continental coasts where sea-surface temperatures are low and the boundary layer is capped by a strong inversion (Klein and Hartmann, 1993). From 35°S to 35°N, stratocumulus clouds have a shortwave plus longwave top of the

50   atmosphere CRE between -150 and -200 W m^{-2} with a 10 to 20% contribution to the net CRE (Oreopoulos and Rossow, 2011).

General Circulation Models have large uncertainties in their estimates of CREs and the associated cloud feedbacks, in part due to their treatment of low-level clouds, particularly stratocumulus (Boucher et al., 2013). The radiative impact of stratocumulus depends on many factors, including the horizontal and vertical distribution of cloud droplets, their size

55   distribution and their number concentration. Stratocumulus properties depend on the number, size, composition and vertical distribution of aerosols, and meteorological parameters such as boundary layer height, air mass history and cloud top instability, all of which can modulate the aerosol loading and influence aerosol-cloud interactions. Increases in aerosols acting as cloud condensation nuclei can increase cloud droplet concentration (N_c) and decrease effective radius (R_e), which increases the cloud optical thickness and shortwave reflectance under conditions of constant liquid water content (LWC)

60   (Twomey, 1974, 1977). Cloud adjustments in response to this aerosol indirect effect can modulate LWC. For example, precipitation suppression in clouds with smaller droplets increases LWC and cloud lifetime, which increases the CRE (Albrecht, 1989). The indirect effect and rapid adjustments in clouds contribute to the effective radiative forcing due to aerosol-cloud interactions (Boucher et al., 2013). Estimates of the effective radiative forcing (-1.2 to 0.0 W m^{-2}) have uncertainties that contribute to the total aerosol radiative forcing, which is "the dominant contributor to overall net Industrial

65   Era forcing uncertainty" (Myhre et al., 2013).

The impact of the indirect effect can depend on above-cloud thermodynamic parameters such as humidity, buoyancy and inversion strength. Shortwave absorption by above-cloud aerosols can increase the buoyancy above cloud tops, inhibit cloud-top entrainment and increase liquid water path (Wilcox, 2010). Depending on the free tropospheric humidity, dry air entrainment can decrease the LWC in clouds with higher N_c due to the indirect effect (Ackerman et al., 2004; Coakley and

70 Walsh, 2002). Enhanced dry air entrainment can weaken the increase in cloud optical thickness associated with smaller droplets (Small et al., 2009; Rosenfeld et al., 2014). A weak inversion can lead to increased cloud-top entrainment and initiate a stratocumulus-to-cumulus transition by deepening and decoupling the boundary layer, and cutting off the surface moisture source (Wood, 2012). Evaporative cooling from mixing cloudy air with the warm and dry free tropospheric air entraining into clouds leads to cloud-top instability, which is the dominant source of turbulence in stratocumulus (Mellado,

75 2017).

One of the largest stratocumulus cloud decks on Earth exists off the coast of Namibia over the southeast Atlantic Ocean with a cloud fraction of over 60% between July and October (Devasthale and Thomas, 2011; Zuidema et al., 2016). Biomass-burning aerosols (BBA) that originate from fires in southern Africa (van der Werf et al., 2010) are transported over the stratocumulus by the southern branch of the African Easterly Jet and overlay the clouds (Adebiyi and Zuidema, 2016).

80 The aerosol layer over time descends and mixes with clouds, affecting cloud microphysical properties and their satellite retrievals (Haywood et al., 2004; Costantino and Breon, 2010). The vertical gap between the aerosol layer and cloud tops changes with longitude, having a maximum separation near 7°E, and has a wide range of values (0 to 2,000 m) with near-zero gap for 48% of the observed scenes during ORACLES (LeBlanc et al., 2020). The southeast Atlantic thus serves as a natural laboratory to examine the effects of varying vertical profiles of above-cloud aerosols on cloud microphysics due to

85 instances of both separation and contact between the BBA layer and the stratocumulus.

BBA over the southeast Atlantic have 500 nm single-scattering albedo ranging between 0.83 and 0.89 (Pistone et al., 2019), which indicates the BBA layer is comprised of absorbing aerosols. The warming associated with shortwave absorption by BBA over the southeast Atlantic can be amplified by the evaporation of cloud droplets, the semi-direct effect (Hansen et al., 1997; Ackerman et al., 2000). Aerosols above a reflective cloud layer absorb more solar radiation than

90 aerosols below or within cloud, which affects cloud formation (Haywood and Shine, 1997) and the region's aerosol direct radiative effect (Keil and Haywood, 2003; Cochrane et al., 2019). Large-eddy simulations indicate that the location of the aerosol layer impacts both the magnitude and sign of the semi-direct forcing (Johnson et al., 2004; McFarquhar and Wang, 2006). For example, aerosols above the boundary layer lead to a stronger inversion and decrease entrainment. Additionally, aerosols within the boundary layer cause cloud evaporation and boundary layer decoupling.

95 The treatment of aerosol effects results in inter-model differences in climate simulations, along with biases in satellite retrievals of clouds and aerosols (Haywood et al, 2004; Brioude et al., 2009; Chand et al., 2009; Coddington et al., 2010; Painemal and Zuidema, 2011). Many large-scale models do not adequately consider cloud microphysical responses to the vertical separation of aerosols when evaluating aerosol-cloud interactions (Hill et al., 2008). The ObseRvations of Aerosols above Clouds and their intEractionS (ORACLES) field campaign provides a unique dataset of in-situ observations of cloud

100 and aerosol properties over the southeast Atlantic (Redemann et al., 2020). The impact of above-cloud BBA on stratocumulus properties is quantified by comparing in-situ cloud measurements from instances with layer separation to instances of contact between the aerosol layer and the clouds.

2 Instrumentation

This study presents in-situ measurements of cloud and aerosol properties acquired during the first Intensive Observation
105 Period (IOP) of ORACLES based at Walvis Bay, Namibia (23°S, 14.6°E). The NASA P-3B aircraft conducted research flights west of Africa over the southeast Atlantic Ocean between 1°W to 15°E and 5°S to 25°S from 27 August to 27 September 2016. The aircraft typically flew 50 m to 7 km above the ocean surface and was equipped with in-situ probes for sampling meteorological conditions, aerosols and clouds (Table 1), among other instrumentation. Water vapor mixing ratio (q) was determined using a chilled-mirror hygrometer as well as the Los Gatos Research $CO/CO_2/H_2O$ gas analyzer. The
110 hygrometer suffered from cold soaking during descents from higher elevation and measured lower q near cloud tops during descents compared to ascents into cloud. Measurements of q from the gas analyzer had to be masked for near and in-cloud samples during both ascents and descents due to residual water in the inlet. Therefore, only hygrometer data collected during ascents are used for the analyses involving q.

The Passive Cavity Aerosol Spectrometer Probe (PCASP) measures aerosol from approximately 0.1 µm to 3.0 µm using
115 three voltage amplifiers; high, middle and low gain stages (Cai et al., 2013). Laboratory sampling of ammonium sulfate particles conducted after the IOP with the PCASP and a Scanning Mobility Particle Size Spectrometer (SMPS) adjusted the PCASP concentration within each amplification stage to match the measured SMPS concentration. Thereby, a low bias within the middle and high gain stages was corrected. A high-resolution time-of-flight aerosol mass spectrometer (AMS) sampled aerosol mass (M_a) and chemistry, including organic aerosols (OA) (Table 1). A Single Particle Soot Photometer
120 (SP2) measured refractory Black Carbon (rBC) concentration and the $CO/CO_2/H_2O$ gas analyzer measured Carbon Monoxide (CO) concentration. The Spectrometers for Sky-Scanning, Sun-Tracking Atmospheric Research (4STAR) was used to measure column aerosol optical depth (AOD) and retrieve trace gas concentrations above the aircraft (Dunagan et al., 2013; LeBlanc et al., 2020).

The suite of in-situ cloud probes included the Cloud and Aerosol Spectrometer (CAS) on the Cloud, Aerosol and
125 Precipitation Spectrometer (CAPS), Cloud Droplet Probe (CDP), Phase Doppler Interferometer (PDI), 2-Dimensional Stereo Probe (2-DS), Cloud Imaging Probe (CIP) on the CAPS, High Volume Precipitation Sampler (HVPS-3) and the CAPS and King hot-wires. These instruments sampled N_c for droplets with diameters ranging from 0.5 to 19200 µm, and the hot-wires measured the bulk LWC. Baumgardner et al. (2017) discuss the general operating characteristics of the in-situ cloud probes and McFarquhar et al. (2017) summarize data processing algorithms. Therefore, only aspects of instrument performance
130 unique to ORACLES 2016 are summarized herein. CDP data were unusable for the entire 2016 IOP due to an optical misalignment issue. Data from the components of CAPS (CAS, CIP and CAPS hot-wire) were not available before 6

September 2016 because of improper seating of the analog to digital interface board, which resulted in no N_c for droplets less than 50 µm in diameter before this flight. The optical lenses were cleaned with isopropyl before each flight, which was especially important during ORACLES since the aircraft frequently flew through the aerosol layer that would deposit soot on

135 optical lenses of the cloud probes. Stuck bits (photodiodes continuously occluded due to soot deposition) on the optical array probes (2-DS and HVPS-3) were masked during each flight to reduce the presence of artifacts. The 2-DS vertical channel consistently had low photodiode voltages below 1.0 volts due to soot deposition on the inside of the receive-side mirror. Therefore, only data from the horizontal channel are used.

The aircraft's true air speed (TAS) was about 15% higher than the TAS measured by a Pitot tube alongside the CIP.

140 Previous work has shown uncertainties with using the Pitot tube TAS to represent airflow near the probes (Lance et al., 2010; Johnson et al., 2012). Therefore, CAPS, 2-DS, and HVPS-3 probes used the aircraft's TAS, in the absence of reliable TAS measured at these probes' locations. CAPS and PCASP data were processed using the Airborne Data Processing and Analysis processing package (Delene, 2011). 2-DS and HVPS-3 data were processed using the University of Illinois/Oklahoma Optical Probe Processing Software (McFarquhar et al., 2018). Droplets measured by the 2-DS and HVPS-

145 3 having aspect ratios greater than 4 or area ratios less than 0.5 were rejected as artifacts because this study focuses on warm clouds with liquid drops sampled above 0°C. Droplets with inter-arrival times less than 6 µs, indicative of intermittently stuck diodes or drizzle breakup, were removed (Field et al., 2006). Out-of-focus hollow particles were reconstructed following Korolev (2007).

Flight profiles consisted of cloud sampling during individual ascents or descents through cloud or during a series of

150 ascents and descents through cloud along a constant heading (sawtooth maneuvers). The droplet size distributions from the CAS and 2-DS were merged at 50 µm in diameter to create a combined 1 Hz spectrum, which was used to calculate N_c, R_e and LWC. While the HVPS-3 sampled droplets larger than 1280 µm in diameter, only three such 1-s samples, with N < 0.005 L^{-1}, were sampled during the cloud profiles from the IOP. A threshold of $N_c > 10$ cm^{-3} and bulk LWC > 0.05 g m^{-3} for 1 Hz measurements was used to define cloud samples (c.f. Lance et al., 2010; Bretherton et al., 2010). The cloud threshold

155 eliminated the inclusion of optically thinner clouds that a lower LWC threshold of 0.01 g m^{-3} would have included (e.g., Heymsfield and McFarquhar, 2001).

3 Observations on 6 September 2016

A case study of the fifth P-3 Research Flight (PRF5) flown on 6 September 2016 was used to examine aerosol and cloud properties sampled under conditions of both contact and separation between the aerosol layer and cloud tops. PRF5 was

160 selected because it had the highest cloud profiling time among the six PRFs with at least eight cloud profiles (Table 2). Four sawtooth maneuvers (S1-S4) were flown during PRF5 (Figure 1) along with four individual cloud profiles (P1-P4). Each sawtooth maneuver consisted of 4-6 individual profiles (Table 2) which were numbered sequentially (e.g., S1-1, S1-2, etc.). South-southeasterly winds (5-8 m s^{-1}) were observed at the surface and at 925 mb (Figure 2a, b). This wind field was

associated with a surface low-pressure system east of the study region centered around 17°S, 13°E that resulted in advection

165 of low clouds toward the northwest. Open- and closed-cells of marine stratocumulus persisted along with pockets of open

cells (POCs) (Figure 1). S1, S2 and S3 were flown along 9°E in closed cells of marine stratocumulus. S4 was flown closer to

the coast in a shallow BL with thin closed-cell stratocumulus (Figure 1) later in the day compared to S1-S3 (Figure 3).

Ambient temperature sampled by the aircraft sensor was 3 to 6 °C higher during S2 and S3 compared to S1 because the 500

mb geopotential height and relative humidity (RH) were higher toward the north (Figure 2b). Cloud top height (Z_T) is

170 identified as the highest altitude satisfying the criteria used to define cloud ($N_c > 10$ cm^{-3} and bulk LWC > 0.05 g m^{-3}). S1,

S2 and S3 had higher Z_T compared to S4 (Figure 3) due to the advection of cold, dry continental air from the southeast and

low RH (< 70%) where S4 was flown which resulted in cloud thinning and a shallower BL (Figure 2b, c).

The aircraft intermittently entered and exited cumulus clouds below the stratocumulus during 33 of the 71 cloud profiles

flown during the IOP (Table 2) which resulted in fluctuating values of N_c and R_e, with bulk LWC < 0.05 g m^{-3}. For example,

175 during S1-3, N_c varied between 10 to 240 cm^{-3} and R_e varied between 3 to 12 µm up to 130 m below where the

stratocumulus base was identified with bulk LWC > 0.05 g m^{-3}. Images from a forward-facing camera on the aircraft contrast

a boundary layer with multiple cloud layers (Figure 4a; image taken at 08:53 UTC) during S1-3 and a shallow, well-mixed

boundary layer capped by stratocumulus (Figure 4b; image taken at 13:16 UTC) during S4-1. It is likely the stratocumulus

layer was decoupled from the surface where S1-3 was flown because the boundary layer was deepened by the entrainment of

180 free tropospheric air. Subsequently, the sub-cloud layer was well-mixed with the surface and topped by shallow cumulus

similar to observations by Wood (2012). The cloud base height (Z_B) for the 33 profiles was determined as the lowest altitude

with $N_c > 10$ cm^{-3} and bulk LWC > 10 g m^{-3} above which a continuous cloud layer was sampled. S4 had lower Z_B (195-249

m) compared to S1 (676-691 m), S2 (534-598 m) and S3 (501-775 m) (Figure 3).

For each sawtooth maneuver, the above- and below-cloud air mass source region was identified using five-day back-

185 trajectories computed using the NOAA Hybrid Single Particle Lagrangian Integrated Trajectory model (Stein et al., 2015)

applied to the National Center for Environmental Prediction Global Data Assimilation System model (Figure 5). The

concentrations listed in Table 3 indicate measurements up to 100 m above and below the clouds averaged across the cloud

profiles for each sawtooth maneuver. The variability in above-cloud M_a and N_a for S1-S4 was driven by the above-cloud air

mass source region. The above-cloud air mass sampled near S1 and S4 originated from the boundary layer from the

190 southeast and the above-cloud air mass sampled near S2 and S3 descended from higher altitudes over the African continent

(Figure 5b, c). The above-cloud OA M_a and N_a for S2 and S3 were over 5 times higher than the corresponding values for S1

and S4 (Table 3). The below-cloud air mass sampled during S1-S4 was advected from the boundary layer from the southeast

(Figure 5a, c). During S1 and S4, the above- and below-cloud rBC and CO concentrations were similar (Table 3) since the

above-cloud air mass also originated from the south east (Figure 5b, c). During S2 and S3, the continental above-cloud air

195 mass had much higher rBC and CO (over 500 cm^{-3} and 190 ppb) compared to the below-cloud air mass from the south east

(below 150 cm^{-3} and 120 ppb). Since OA, rBC and CO are indicators of combustion, this suggests the continental above-

cloud air mass had greater exposure to biomass-burning products compared to the air masses from the south east. S2 and S3

also had higher below-cloud rBC and CO compared to S1 and S4 (Table 3) which suggests the BBA with high N_a within 100 m above clouds could be mixing into the cloud layer and polluting the BL.

200   Every sawtooth maneuver was preceded by a 5- to 10-minute constant-altitude flight leg about 100 m above the cloud layer to retrieve the above-cloud aerosol optical depth (AOD) using 4STAR. Average above-cloud AOD at 550 nm within 50 km of the sampling locations for S1-S4 ranged between 0.33 and 0.49, indicating the BBA layer was located at some altitude above the clouds sampled during S1-S4. During S1, above-cloud $N_a < 500$ cm^{-3} was sampled up to 200 m above cloud tops (Figure 3) which indicates the BBA layer was separated from cloud tops. During S4, the level of above-cloud N_a
205   > 500 cm^{-3} was identified over 200 m above cloud tops indicating a similar separation. Therefore, cloud profiles flown during S1 and S4 were classified as *separated* profiles. During S2 and S3, the level of above-cloud $N_a > 500$ cm^{-3} was located within 100 m above cloud tops and the BBA layer was likely in contact with the cloud tops. Therefore, cloud profiles flown during S2 and S3 were classified as *contact* profiles.

    Since Z_B and cloud thickness (H) varied between profiles, N_c, R_e, and LWC were examined as a function of normalized
210   height above cloud base (Z_N), where $Z_N = (Z - Z_B)/(Z_T - Z_B)$ and varied from 0 (cloud base) to 1 (cloud top). Measurements from the four sawtooth maneuvers were compared following McFarquhar et al. (2007), and divided into 10 Z_N bins where each bin represented 10% of the cloud layer (Figure 6). For example, the bin with $0 < Z_N < 0.1$ (represented by the midpoint, $Z_N = 0.05$) included data collected over the bottom 10% of the cloud layer. For *separated* profiles, droplet nucleation occurred near cloud base with the median N_c increasing up to $Z_N = 0.25$ (S1: 132 to 179 cm^{-3}, S4: 23 to 85 cm^{-3}). The impact
215   of droplet nucleation decreased above cloud base ($Z_N = 0.25$ to 0.75) and median N_c increased by up to 30 cm^{-3} for S1 and decreased by up to 15 cm^{-3} for S4 (Figure 6a). Condensational growth occurred over these levels as the median R_e increased with Z_N (Figure 6b). The median N_c decreased near cloud top ($Z_N = 0.75$ to 0.95) due to droplet evaporation resulting from cloud-top entrainment mixing between cloudy and non-cloudy air. *Contact* profiles (S2 and S3) had higher median N_c at cloud base compared to *separated* profiles which decreased with height up to $Z_N = 0.25$ (S2: 190 to 169 cm^{-3}, S3: 180 to 131
220   cm^{-3}). The median N_c for S2 and S3 increased by up to 43 cm^{-3} over $Z_N = 0.25$ to 0.75 and decreased near cloud top due to droplet evaporation. S4 had the lowest N_c at cloud base because the below-cloud M_a and N_a for S4 were over a factor of 3 lower than the corresponding values for S1-S3 (Table 3).

    Consistent with condensational growth and collision-coalescence, median R_e increased with Z_N from cloud base to top, from 6.0 µm to 6.7 µm, 4.6 to 6.9 µm, 4.9 to 8.3 µm and 8.7 to 9.9 µm for S1-S4, respectively (Figure 6b). S1 and S4 had
225   higher median R_e at cloud base due to higher drizzle (droplets greater than 50 µm in diameter) concentrations (41 and 31 L^{-1}) compared to S2 and S3 (14 and 18 L^{-1}). For S4, drizzle concentration decreased near cloud base which led to the decrease in median R_e. The median LWC increased with height up to at least $Z_N = 0.75$, and decreased near cloud tops due to droplet evaporation (Figure 6c). The LWC for each sawtooth maneuver was lower than the adiabatic LWC (aLWC) due to cloud-top entrainment mixing and the ratio of LWC to aLWC was used to quantify the degree of mixing. Lower LWC/aLWC for S2
230   and S3 (0.37 and 0.41) compared to S1 and S4 (0.51 and 0.55) indicated that *contact* profiles had greater mixing between cloudy and non-cloudy air in the cloud layer, on average. The boundary layer was capped by an inversion with warmer, drier

air above the clouds. During S1-S4, the temperature increased above cloud top by 10.3, 9.3, 8.9 and 1.5°C, and the total water mixing ratio decreased by 6.2, 5.4, 2.3 and 0.4 g kg^{-1}, respectively (Figure 7). The decreases in N_c and LWC near stratocumulus tops have been attributed to cloud-top entrainment of the overlying warm and sub-saturated air (Wood, 2012).

235 Droplet evaporation due to the entrainment mixing resulted in decreases of 14%, 28%, 12% and 26% in the median N_c near cloud tops during S1-S4, respectively.

N_c and R_e were compared between sawtooth maneuvers and the differences reported hereafter refer to 95% confidence intervals for the difference in the variable means (based on a two-sample t-test, $p < 0.02$). Between the *contact* profiles, S2 had significantly higher N_c (differences of 37 to 56 cm^{-3}) compared to S3. This was despite having statistically insignificant

240 differences in below-cloud N_a, a greater fractional decrease in median N_c near cloud top compared to S3, and greater entrainment mixing (lower LWC/aLWC). S2 had significantly higher above-cloud N_a compared to S3 and the mixing of above-cloud air with high N_a likely resulted in droplet nucleation above cloud base, where the median N_c for S2 increased from 169 to 220 cm^{-3} over $Z_N = 0.25$ to 0.75. Between the *separated* profiles, S1 had significantly higher N_c (differences of 108 to 126 cm^{-3}) which could be attributed to significantly higher above-cloud N_a and greater entrainment mixing during S1

245 compared to S4. However, these differences could also be due to the meteorological differences at their sampling locations (lower BL height, RH and 500 mb geopotential height, ΔT and Δq_T for S4) or the significantly higher below-cloud N_a for S1 compared to S4.

Contact profiles had significantly higher N_c (differences of 45 to 61 cm^{-3}) and lower R_e (differences of 1.4 to 2.0 µm) compared to *separated* profiles. *Contact* profiles also had significantly higher above-cloud N_a and greater entrainment

250 mixing in the cloud layer (lower LWC/aLWC). Higher N_c in the cloud layer due to entrainment mixing of free tropospheric air with significantly higher above-cloud N_a provided evidence of the aerosol indirect effect due to the presence of above-cloud BBA. However, *contact* profiles also had significantly higher below-cloud N_a (differences of 145 to 190 cm^{-3}) which could have contributed to the higher N_c relative to *separated* profiles. Therefore, a statistical analysis was conducted with a larger number of profiles to confidently attribute these differences in N_c and R_e to the vertical distance between the above-

255 cloud BBA layer and cloud tops. Building on this case study, 71 cloud profiles flown on six flights between 6 and 25 September 2016 were examined and the impact of above-cloud BBA on the free tropospheric humidity and buoyancy across cloud tops was explored. 61 profiles were further classified into four new regimes based on below-cloud N_a to quantify the differences in N_c between *contact* and *separated* profiles within boundary layers with similar below-cloud N_a.

4 Statistical Analysis

260 On 10, 12 and 25 September, the P-3 took off from Walvis Bay, Namibia (23˚S, 14.6˚E) and flew north-west from 23˚S, 13.5˚E toward 10˚S, 0˚E, returning along the same track (Figure 8). Different tracks were followed on 6, 14 and 20 September which included meridional legs along 9°E, 7.5°E and 9°E, and 9°E and 10.5°E, respectively. Meteorological conditions on 10, 12 and 14 September were similar to the conditions described for the case study. South-southeasterly

surface winds were associated with a surface low-pressure system over Africa. The surface wind speeds varied between 5 to
265   10 m s^{-1} depending on the pressure gradient between the continental low and a surface high toward the southwest. A region
of 925 mb RH < 60% persisted along the coast due to dry air advection from Africa. A different meteorological setup on 20
September had westerly surface winds and easterly winds at 925 mb. The aerosol plume was sampled immediately above the
boundary layer (600 m) as warm surface air was overlaid by drier, polluted air from the continent. The continental surface
low was located farther south on 25 September compared to other flight days with the region of low 925 mb RH to the south
270   of the flight track. The study region had RH >60% with south-southeasterly surface winds and southerly 925 mb winds.

The BBA layer with above-cloud N_a > 500 cm^{-3} was sampled during each flight with variability in its vertical location
(Table 4). Only *separated* profiles were flown on 10 and 14 September (Table 2) when the BBA layer and cloud tops were
separated by over 600 and 1500 m, respectively (Table 4). On 12 September, P1 had N_a > 500 cm^{-3} within 75 above cloud
tops and was classified as a *contact* profile while P2 and S1 were classified as *separated* profiles. On 20 September, each
275   profile had above-cloud AOD > 0.4 and was classified as a *contact* profile. On 25 September, the profiles had above-cloud
AOD > 0.27 and each profile (except from a sawtooth near 11°S, 1°E) was classified as a *contact* profile. Since clouds
sampled on different flight days had variable Z_B and Z_T (Figure 9), vertical profiles of N_c, R_e and LWC from the *contact* and
separated profiles were compared as a function of Z_N.

The frequency distributions of N_c, R_e and LWC as a function of Z_N were examined using violin plots (Hintze and
280   Nelson, 1998; Wang et al., 2020) where the width of the shaded area represents the proportion of data there. The average N_c
for *contact* profiles was significantly higher than the average N_c for *separated* profiles (differences of 60 to 68 cm^{-3}). During
separated profiles, the median N_c had little variability up to Z_N = 0.75 (114 to 122 cm^{-3}) and decreased thereafter with Z_N to
73 cm^{-3} due to droplet evaporation (Figure 10a). During *contact* profiles, the median N_c decreased slightly up to Z_N = 0.25
(183 to 174 cm^{-3}), increased to 214 cm^{-3} at Z_N = 0.75, and decreased near cloud top to 157 cm^{-3} due to droplet evaporation.
285   *Contact* profiles had significantly lower R_e than the *separated* profiles (differences of 1.1 to 1.3 µm) and the median R_e
increased with Z_N from 4.9 to 7.0 µm for *contact* and 6.6 to 8.6 µm for *separated* profiles (Figure 10b). The differences in R_e
were likely due to the significantly lower drizzle concentrations for *contact* profiles (differences of 5 to 20 L^{-1}).

The average LWC for *contact* and *separated* profiles were within 0.01 g m^{-3}, and the median LWC increased with Z_N to
0.23 g m^{-3} at Z_N = 0.85 for *contact* and 0.21 g m^{-3} at Z_N = 0.75 for *separated* profiles (Figure 10c). *Contact* profiles had
290   lower LWC/aLWC in the cloud layer (0.45) compared to *separated* profiles (0.57) which suggests there was greater
entrainment mixing during *contact* profiles, on average. However, droplet evaporation near cloud top had a stronger impact
on *separated* profiles as the median LWC decreased to 0.16 g m^{-3} for *separated* and 0.20 g m^{-3} for *contact* profiles (Figure
10c). *Separated* profiles had a greater decrease in LWC/aLWC near cloud top (0.41 to 0.26) compared to *contact* profiles
(0.38 to 0.30) and greater fractional decreases in median N_c and LWC (40% and 16%) compared to *contact* profiles (25%
295   and 9%). The stronger impact of droplet evaporation during *separated* profiles contributed to the differences between N_c for
contact and *separated* profiles. Buoyancy and humidity across cloud tops are determined to explore the cloud-top
entrainment mechanisms resulting in the differential impact of droplet evaporation for these profiles.

Cloud-top instability is the dominant source of turbulence in stratocumulus with evaporative cooling being a key driver of instability (Mellado, 2017). Evaporative cooling in a mixture of dry and cloudy air near cloud top generates negatively

300 buoyant air mixtures which further enhances mixing and leads to an entrainment feedback called Cloud Top Entrainment Instability or CTEI (Kuo and Schubert, 1988). Under such conditions, negative buoyancy leads to an unstable feedback, unlike the conventional association of negative buoyancy with atmospheric stability. The critical condition for cloud-top stability from Kuo and Schubert (1988) is shown in Eq. (1),

$$\Delta\theta_e > k\left(\frac{L_v}{c_p}\right)\Delta q_T \tag{1}$$

305 where k is the CTEI parameter, θ_e is the equivalent potential temperature, L_v is the latent heat of vaporization, and c_p is the specific heat capacity of air at constant pressure. The Δ operator represents gradients across the cloud-top, defined here as the difference between θ_e (or q_T) measured 100 m above cloud top and the vertical average of θ_e (or q_T) over the top 100 m of the profile. Following Eq. (13) from Kuo and Schubert (1988), k > 0.23 indicates negative buoyancy across cloud tops. Water vapor mixing ratio (q) measured by the chilled-mirror hygrometer was used to calculate θ_e and q_T. Since lower Δq_T

310 was sampled during descents into cloud due to condensation on the hygrometer, k-values for descents were determined to be measurement artifacts and not usable here.

All *separated* profiles (except PRF5 S1-3 and S4-1, 3, 5) laid within the region of cloud-top instability (k > 0.23) on a $\Delta\theta_e$ - Δq_T plane (Figure 11) and showed negative buoyancy across cloud tops. During PRF5 S1-3, low $\Delta\theta_e$ was sampled due to higher above-cloud humidity associated with the presence of $N_a > 100$ cm^{-3} within 50 m above cloud tops. During PRF5

315 S4, a weak cloud-top inversion led to positive $\Delta\theta_e$ and $\Delta q_T < -2$ g kg^{-1} (Fig. 7). For the remaining *separated* profiles, negative buoyancy across cloud tops led to forced descent of dry, free tropospheric air into the clouds. Since the free tropospheric air was warmer and drier than the cloudy air, droplet evaporation led to the decreases in median N_c and LWC near cloud top. The positive evaporative cooling feedback and greater Δq_T compared to *contact* profiles (Figure 11) explain the stronger impact of droplet evaporation on median N_c and LWC for *separated* profiles. While evaporative cooling

320 triggered the CTEI feedback, the clouds persisted consistent with cloud-top radiative cooling or surface evaporation leading to boundary layer moistening (Lock, 2009; Mellado, 2017). All *contact* profiles (except PRF13 S1-3) laid within the region of cloud-top stability and showed positive buoyancy across cloud tops. Entrainment mixing for these profiles likely occurred when the clouds penetrated the inversion. In the presence of above-cloud BBA, the above-cloud air was more humid and the above-cloud N_a were significantly higher compared to *separated* profiles (differences of 768 to 831 cm^{-3}). *Contact* profiles

325 had greater entrainment mixing compared to *separated* profiles and the median N_c increased with height over $Z_N = 0.25$ to 0.75. It is likely the entrainment of BBA into clouds resulted in additional droplet nucleation over these Z_N levels.

Therefore, weaker droplet evaporation near cloud top and additional droplet nucleation above cloud base in the presence of above-cloud BBA likely contributed to the differences between N_c for *contact* and *separated* profiles. However, *contact* profiles also had significantly higher below-cloud N_a (differences of 93 to 115 cm^{-3}) which could have contributed to these

330 differences. Therefore, 28 *contact* and 33 *separated* profiles were classified into four new regimes to investigate the

contribution of below-cloud N_a relative to the impact of above-cloud BBA. The new regimes were termed Contact-high N_a (C-H), Contact-low N_a (C-L), Separated-high N_a (S-H) and Separated-low N_a (S-L) to represent *contact* or *separated* profiles within a high- or low-N_a boundary layer. Boundary layers were classified based on maximum below-cloud N_a and statistical differences between the average above- and below-cloud N_a, N_c and R_e were quantified (Table 5). There were no *contact* or

335   *separated* profiles with maximum below-cloud $N_a < 100$ cm^{-3} and only 3 out of 28 *contact* profiles (with 139 1-Hz measurements) had maximum below-cloud $N_a < 200$ cm^{-3}. Thus, higher thresholds were used to define a high-N_a boundary layer for adequate sample sizes.

    With a threshold of maximum below-cloud $N_a > 300$ cm^{-3} for high-N_a boundary layers, 22 *contact* and 13 *separated* profiles laid within high-N_a boundary layers. C-L profiles had significantly lower below-cloud N_a compared to S-L profiles

340   but the differences between N_c were statistically insignificant (Table 5). The median N_c for C-L and S-L profiles were within 10 cm^{-3} over $Z_N = 0.25$ to 0.85 with little variability (< 20 cm^{-3}) as a function of Z_N (Figure 12a). In the presence of higher above-cloud N_a, C-L profiles had a smaller decrease in median N_c due to droplet evaporation (18 cm^{-3}) compared to S-L profiles (35 cm^{-3}). C-H profiles had significantly higher above- and below-cloud N_a which led to significantly higher N_c compared to S-H profiles (Table 5). The median N_c for S-H profiles had little variability (109 to 113 cm^{-3}) up to $Z_N = 0.65$,

345   increased to 136 cm^{-3} at $Z_N = 0.75$, and decreased near cloud top due to droplet evaporation. The median N_c for C-H profiles increased by 41 cm^{-3} over $Z_N = 0.25$ to 0.75 and the difference between median N_c for C-H and S-H profiles increased over these levels. The differences in median N_c increased further near cloud top due to droplet evaporation as C-H profiles had a smaller decrease in median N_c (32 cm^{-3}) compared to S-H profiles (56 cm^{-3}) .

    For a higher threshold, 20 *contact* and 11 *separated* profiles laid within high-N_a (> 350 cm^{-3}) boundary layers. C-L

350   profiles had higher N_c despite insignificant differences between the below-cloud N_a (Table 5). The median N_c for C-L and S-L profiles had little variability (< 20 cm^{-3}) as a function of Z_N and differed by up to 25 cm^{-3} over $Z_N = 0.05$ to 0.85 (Figure 12b). The difference in median N_c increased near cloud top as C-L profiles had a smaller decrease due to droplet evaporation (8 cm^{-3}) compared to S-L profiles (32 cm^{-3}). C-H profiles had significantly higher above- and below-cloud N_a which led to significantly higher N_c compared to S-H profiles (Table 5). The median N_c increased with height over $Z_N = 0.25$ to 0.75 by

355   19 cm^{-3} for S-H and 39 cm^{-3} for C-H profiles. The C-H profiles had a smaller decrease in median N_c near cloud top (29 cm^{-3}) compared to S-H (66 cm^{-3}). The threshold to define high-N_a boundary layers was not increased further because there were little differences between the below-cloud N_a for *contact* profiles within high- and low-N_a boundary layers.

    These results suggest the differences between N_c for *contact* and *separated* profiles were primarily driven by the stronger impact of droplet evaporation on *separated* profiles (especially within low-N_a boundary layers where most of the

360   *separated* profiles were sampled). There was evidence of droplet nucleation in the middle of the cloud layer ($Z_N = 0.25$ to 0.75) within high-N_a boundary layers. Subsequently, the differences between N_c within high-N_a boundary layers were due to higher below-cloud N_a, additional nucleation above cloud base, and weaker droplet evaporation in the presence of above-cloud BBA. *Contact* profiles were more frequently located in high-N_a boundary layers, and it is likely the presence of above-cloud BBA affected below-cloud N_a. This is supported by the sampling of significantly higher below-cloud CO during

365   *contact* profiles compared to *separated* profiles (differences of 13 to 16 ppb). *Contact* profiles with below-cloud CO > 100 ppb corresponded to higher median above-cloud CO (240 ppb) compared to *contact* profiles with lower below-cloud CO (104 ppb). The sensitivity of the comparisons within this study to using different thresholds to locate the BBA layer (other than 500 cm^{-3}) and to define "separation" between the aerosol layer and cloud tops (other than 100 m) is discussed in Appendix A.

370   **5 Conclusions**

This study provides observational evidence of the aerosol indirect effect on marine stratocumulus cloud properties due to contact between above-cloud biomass burning aerosols and stratocumulus cloud tops over the southeast Atlantic Ocean. Biomass-burning aerosols overlay marine stratocumulus clouds there with variability in the vertical separation (0 to 2000 m) between the aerosol layer and cloud tops. The presence of biomass-burning aerosols immediately above cloud tops impacts

375   N_c, R_e, and LWC through cloud-top entrainment and increases the free tropospheric temperature and humidity. In-situ measurements of cloud and aerosol properties from 6 research flights during the NASA ORACLES field campaign in September 2016 are presented. Meteorological conditions and the vertical profiles of N_c, R_e, LWC and above- and below-cloud N_a are examined for a case study of 6 September 2016. Thinner clouds with lower cloud base and top heights were sampled closer to the coast due to lower relative humidity and boundary layer height compared to clouds sampled along 9°E.

380   For 33 cloud profiles, cloud-top entrainment deepened the boundary layer, decoupled the stratocumulus layer from the surface and resulted in cumulus formation below the stratocumulus. The vertical profiles of cloud (N_c, R_e and LWC) and thermodynamic (q_T and T) properties sampled on 6 September 2016 were consistent with observations of stratocumulus-topped boundary layers capped by an inversion with warm, dry free tropospheric air above the clouds (Wood, 2012).

Above-cloud air masses originating from Africa were composed of biomass-burning products (OA, rBC and CO) with

385   higher N_a compared to above-cloud air masses originating from the boundary layer over the southeast Atlantic Ocean. 30 *contact* profiles were flown where the level of N_a > 500 cm^{-3} was within 100 m above cloud tops and 41 *separated* profiles were flown where N_a > 500 cm^{-3} was sampled at least 100 m above cloud tops. For *contact* profiles, the average N_c in the cloud layer was up to 68 cm^{-3} higher, the average R_e was up to 1.3 µm lower, and the average LWC was within 0.01 g m^{-3} compared to *separated* profiles. During the *contact* profiles, q_T decreased across cloud tops by up to 6 g kg^{-1}. With positive

390   buoyancy across cloud tops, mixing between free tropospheric and cloudy air occurred when clouds penetrated the inversion and median N_c and LWC decreased by 25% and 9% near cloud tops due to droplet evaporation. The entrainment mixing of free tropospheric air with N_a > 500 cm^{-3} likely resulted in droplet nucleation above cloud base and the median N_c for *contact* profiles increased within the middle of the cloud layer. During *separated* profiles, q_T decreased across cloud tops by up to 9 g kg^{-1}. With negative buoyancy across cloud tops, forced descent of drier free tropospheric air into the clouds resulted in a

395   positive feedback of evaporative cooling, and median N_c and LWC decreased by 30% and 16% due to droplet evaporation. The median N_c during *separated* profiles had little variability with height above cloud base before decreasing near cloud top

due to droplet evaporation. Therefore, *contact* profiles had higher N_c due to a combination of weaker droplet evaporation near cloud tops and additional droplet nucleation above cloud base in the presence of above-cloud biomass-burning aerosols.

400   Biomass-burning aerosols located immediately above cloud top mixed into the cloud and polluted the boundary layer. During the case study, sawtooth maneuvers with *contact* profiles had higher below-cloud rBC and CO concentrations (by up to 60 cm^{-3} and 30 ppb) compared to maneuvers with *separated* profiles. Among the 71 profiles across six research flights, *contact* profiles had significantly higher below-cloud CO and N_a compared to *separated* profiles due to the contact between biomass-burning aerosols and cloud tops. 28 *contact* and 33 *separated* profiles were further classified as Contact-high N_a (C-H), Contact-low N_a (C-L), Separated-high N_a (S-H) and Separated-low N_a (S-L) to represent *contact* or *separated* profiles

405   within high-N_a (> 350 cm^{-3}) or low-N_a (< 350 cm^{-3}) boundary layers. C-L profiles had up to 34.9 cm^{-3} higher average N_c and up to 0.9 μm lower average R_e compared to S-L profiles despite statistically insignificant differences between the below-cloud N_a. C-H profiles had up to 70.5 cm^{-3} higher below-cloud N_a, up to 88.4 cm^{-3} higher N_c, and up to 1.6 μm lower R_e compared to S-H profiles. The differences between *contact* and *separated* profiles in low-N_a boundary layers were primarily driven by weaker droplet evaporation in the presence of above-cloud biomass-burning aerosols. For clouds within high-N_a

410   boundary layers, the median N_c increased with height in the middle of the cloud layer, likely due to droplet nucleation above cloud base. Consequently, the differences between *contact* and *separated* profiles within high-N_a boundary layers were driven by a combination of higher below-cloud N_a, droplet nucleation above cloud base, and weaker droplet evaporation in the presence of biomass-burning aerosols above cloud tops.

    In-situ observations of significant changes in N_c and R_e due to contact with the above-cloud biomass-burning aerosol

415   layer motivate future investigations of aerosol impacts on drizzle formation and the onset of precipitation (Pawlowska and Brenguier, 2003; Feingold and Siebert, 2009; Sorooshian et al., 2009). Precipitation suppression due to the entrainment of overlying aerosols into clouds is likely to impact stratocumulus to cumulus transitions (Yamaguchi et al., 2015) and modulate the reversible transitions between closed and open cellular stratocumulus (Abel et al., 2020; Feingold et al., 2015). The addition of in-situ observations from ORACLES deployments in August 2017 and October 2018 (Redemann et al.,

420   2020) also provide a larger dataset to evaluate cloud and precipitation retrievals (Dzambo et al., 2019; Painemal et al., 2020) and investigate aerosol-cloud-precipitation interactions over the southeast Atlantic over a broader range of environmental conditions.

Appendix A

    Cloud profiles were classified as *contact* or *separated* according to whether above-cloud N_a greater than 500 cm^{-3} was

425   measured at a level within 100 m above cloud tops. The classification of cloud profiles remained unchanged when $N_a = 400$ cm^{-3} instead of $N_a = 500$ cm^{-3} was used to locate the aerosol layer. When the level of $N_a = 300$ cm^{-3} was used, 3 of the 26 *separated* profiles (PRF5 S1, PRF5 P2 and PRF7 P6) switched to the *contact* regime. The qualitative results were unchanged as *contact* profiles had higher N_c (differences of 63 to 71 cm^{-3}) and lower R_e (differences of 1.1 to 1.3 μm) compared to

Atmospheric
Chemistry
and Physics
Discussions
Open Access
EGU

separated profiles. When a level of $N_a = 600$ cm^{-3} was used, 2 of the 15 *contact* profiles (PRF5 P1 and P3) switched to the

430   *separated* regime and *contact* profiles had higher N_c (differences of 59 to 67 cm^{-3}) and lower R_e (differences of 1.0 to 1.2 µm). No additional changes were observed upon changing the definition of the BBA layer. Thus, the results obtained were robust as relates to this threshold.

A gap of 100 m was used to define separation between the BBA and the clouds. When this gap was decreased to 50 m, 4 of the 15 *contact* profiles (PRF5 P4, PRF8 P1 and PRF11 S1, P6) switched to the *separated* regime and the *contact* regime

435   had higher N_c (differences of 50 to 59 cm^{-3}) and lower R_e (differences of 0.67 to 0.92 µm). There was no change in the profile classification when increasing the gap from 100 m to 200 m. On increasing the gap to 300 m, PRF5 S4 switched to the *contact* regime and contact profiles had higher N_c (differences of 36 to 45 cm^{-3}) and lower R_e (differences of 0.4 to 0.6 µm). The same profile switches were observed when the definition of the gap was varied between 50 and 300 m for a threshold of above-cloud $N_a = 400$ cm^{-3} to locate the BBA layer. Thus, the findings were robust as relates to the choice of

440   these thresholds.

Atmospheric
Chemistry
and Physics
Discussions

References

Abel, S. J., Barrett, P. A., Zuidema, P., Zhang, J., Christensen, M., Peers, F., Taylor, J. W., Crawford, I., Bower, K. N., and
Flynn, M.: Open cells exhibit weaker entrainment of free-tropospheric biomass burning aerosol into the southeast
465   Atlantic boundary layer, Atmos. Chem. Phys., 20, 4059–4084, https://doi.org/10.5194/acp-20-4059-2020, 2020.

Ackerman, A. S., Kirkpatrick, M. P., Stevens, D. E., and Toon, O. B.: The impact of humidity above stratiform clouds on
indirect climate forcing, Nature, 432, 1014–1017, 2004.

Ackerman, A. S., Toon, O. B., Stevens, D. E., Heymsfield, A. J., Ramanathan, V., and Welton, E. J.: Reduction of tropical
cloudiness by soot, Science, 288, 1042–1047, 2000

470   Albrecht, B.: Aerosols, Cloud Microphysics, and Fractional Cloudiness, Science, 245, 1227–1230, 1989.

Baumgardner, D., Jonsson, H., Dawson, W., Connor, D. O., and Newton, R.: The cloud, aerosol and precipitation
spectrometer (CAPS): A new instrument for cloud investigations, Atmos. Res., 59, 59–60, 2001.

Baumgardner, D., Abel, S. J., Axisa, D., Cotton, R., Crosier, J., Field, P., Gurganus, C., Heymsfield, A., Korolev, A.,
Kraemer, M., Lawson, P., McFarquhar, G., Ulanowski, Z., and Um, J.: Cloud ice properties: in situ measurement
475   challenges, Meteor. Monographs, 58, 9.1–9.23, https://doi.org/10.1175/AMSMONOGRAPHS-D-16-0011.1, 2017.

Boucher, O., Randall, D., Artaxo, P., Bretherton, C., Feingold, G., Forster, P., Kerminen, V.-M., Kondo, Y., Liao, H.,
Lohmann, U., Rasch, P., Satheesh, S. K., Sherwood, S., Stevens, B., and Zhang, X. Y.: Clouds and Aerosols. In: Climate
Change 2013: The Physical Science Basis, Contribution of Working Group I to the Fifth Assessment Report of the
Intergovernmental Panel on Climate Change, edited by: Stocker, T. F., Qin, D., Plattner, G.-K., Tignor, M., Allen, S. K.,
480   Boschung, J., Nauels, A., Xia, Y., Bex, V., and Midgley, P. M., Cambridge University Press, Cambridge, United
Kingdom and New York, NY, USA, 571–657, 2013.

Bretherton, C. S., Wood, R., George, R. C., Leon, D., Allen, G., and Zheng, X.: Southeast Pacific stratocumulus clouds,
precipitation and boundary layer structure sampled along 20◦ S during VOCALS-REx, Atmos. Chem. Phys., 10, 10639–
10654, doi:10.5194/acp-10-10639-2010, 2010.

485   Brioude, J., Cooper, O. R., Feingold, G., Trainer, M., Freitas, S. R., Kowal, D., Ayers, J. K., Prins, E., Minnis, P., McKeen,
S. A., Frost, G. J., and Hsie, E.-Y.: Effect of biomass burning on marine stratocumulus clouds off the California coast,
Atmos. Chem. Phys., 9, 8841–8856, doi:10.5194/acp-9-8841-2009, 2009.

Cai, Y., Montague, D. C., Mooiweer-Bryan, W., and Deshler, T.: Performance characteristics of the ultra-high sensitivity
aerosol spectrometer for particles between 55 and 800 nm: Laboratory and field studies, J. Aerosol Sci., 39, 759–769,
490   doi:10.1016/j.jaerosci.2008.04.007, 2008.

Cai, Y., Snider, J. R., and Wechsler, P.: Calibration of the passive cavity aerosol spectrometer probe for airborne
determination of the size distribution, Atmos. Meas. Tech., 6, 2349–2358, doi:10.5194/amt-6-2349-2013, 2013.

Chand, D., Wood, R., Anderson, T. L., Satheesh, S. K., and Charlson, R. J.: Satellite-derived direct radiative effect of
aerosols dependent on cloud cover, Nature Geosci., 2, 181–184, 2009.

495 Chuang, P. Y., Saw, E. W., Small, J. D., Shaw, R. A., Sipperley, C. M., Payne, G. A., and Bachalo, W.: Airborne Phase
      Doppler Interferometry for Cloud Microphysical Measurements, Aerosol Sci. Technol., 42, 685–703, 2008.

Coakley Jr., J. A. and Walsh, C. D.: Limits to the aerosol indirect radiative forcing derived from observations of ship tracks,
      J. Atmos. Sci., 59, 668–680, 2002.

Cochrane, S. P., Sebastian Schmidt, K., Chen, H., Pilewskie, P., Kittelman, S., Redemann, J., Leblanc, S., Pistone, K.,
500   Kacenelenbogen, M., Segal Rozenhaimer, M., Shinozuka, Y., Flynn, C., Platnick, S., Meyer, K., Ferrare, R., Burton, S.,
      Hostetler, C., Howell, S., Freitag, S., Dobracki, A. and Doherty, S.: Above-cloud aerosol radiative effects based on
      ORACLES 2016 and ORACLES 2017 aircraft experiments, Atmos. Meas. Tech., 12(12), 6505–6528, doi:10.5194/amt-
      12-6505-2019, 2019.

Coddington, O. M., Pilewskie, P., Redemann, J., Platnick, S., Russell, P. B., Schmidt, K. S., Gore, W. J., Livingston, J.,
505   Wind, G. and Vukicevic, T.: Examining the impact of overlying aerosols on the retrieval of cloud optical properties
      from passive remote sensing, J. Geophys. Res., 115(D10), D10211, doi:10.1029/2009JD012829, 2010.

Costantino, L. and Breon, F.-M.: Analysis of aerosol-cloud inter- ´action from multi-sensor satellite observations, Geophys.
      Res. Lett., 37, L11801, doi:10.1029/2009GL041828, 2010.

Delene, D. J.: Airborne Data Processing and Analysis Software Package, Earth Science Informatics, 4(1), 29-44, 2011.

510 Devasthale, A. and Thomas, M. A.: A global survey of aerosol-liquid water cloud overlap based on four years of CALIPSO-
      CALIOP data, Atmos. Chem. Phys., 11, 1143–1154, https://doi.org/10.5194/acp-11-1143-2011, 2011.

Drewnick, F., Hings, S., De Carlo, P., Jayne, J., Gonin, M., Fuhrer, K., Weimer, S., Jimenez, J., Demerjian, K., Borrmann,
      S., and Worsnop, D.: A new time-of-flight aerosol mass spectrometer (TOF-AMS) – Instrument description and first
      field deployment, Aerosol Sci. Technol., 39, 637–658, doi:10.1080/02786820500182040, 2005.

515 Dunagan, S. E., Johnson, R., Zavaleta, J., Russell, P. B., Schmid, B., Flynn, C., Redemann, J., Shinozuka, Y., Livingston, J.,
      and Segal-Rosenhaimer, M.: Spectrometer for Sky-Scanning Sun-Tracking Atmospheric Research (4STAR): Instrument
      Technology, Remote Sensing, 5, 3872–3895, https://doi.org/10.3390/rs5083872, 2013.

Dzambo, A. M., L'Ecuyer, T., Sy, O. O., and Tanelli, S.: The Observed Structure and Precipitation Characteristics of
      Southeast Atlantic Stratocumulus from Airborne Radar During ORACLES 2016-17. Journal of Applied Meteorology
520   and Climatology, doi: 10.1175/jamc-d-19-0032.1, 2019.

Feingold, G. and Siebert, H.: Cloud – Aerosol Interactions from the Micro to the Cloud Scale, from the Strungmann Forum
      Report, Clouds in the Perturbed Climate System: Their Relationship to Energy Balance, Atmospheric Dynamics, and
      Precipitation, edited by: Heintzenberg, J. and Charlson, R. J., MIT Press, ISBN 978-0-262-01287-4, 2009.

Feingold, G., Koren, I., Yamaguchi, T., and Kazil, J.: On the reversibility of transitions between closed and open cellular
525   convection, Atmos. Chem. Phys., 15, 7351–7367, https://doi.org/10.5194/acp-15-7351-2015, 2015.

Field, P., Heymsfield, A., and Bansemer, A.: Shattering and particle interarrival times measured by optical array probes in
      ice clouds, J. Atmos. Ocean. Tech., 23, 1357–1371, 2006.

Hansen, J., Sato, M., and Ruedy, R.: Radiative forcing and climate response, J. Geophys. Res., 102, 6831–6864, 1997.

Hartmann, D. L., Ockert-Bell, M. E., and Michelsen, M. L.: The effect of cloud type on Earth's energy balance: Global
530   analysis, J. Climate, 5, 1281–1304, 1992

Haywood, J. M. and Shine, K. P.: Multi-spectral calculations of the radiative forcing of tropospheric sulfate and soot
aerosols using a column model, Q. J. R. Meteorol. Soc., 123, 1907–1930, 1997.

Haywood, J. M., Osborne, S. R., and Abel, S. J.: The effect of overlying absorbing aerosol layers on remote sensing
retrievals of cloud effective radius and cloud optical depth, Q. J. R. Meteorol. Soc., 130, 779–800, 2004.

535 Heymsfield, A.J., and McFarquhar, G.M.: Microphysics of INDOEX clean and polluted trade wind cumulus clouds. J.
Geophys. Res., 106, 28653-28673, 2001.

Hill, A. A., Dobbie, S., and Yin, Y.: The impact of aerosols on nonprecipitating marine stratocumulus, I: Model description
and prediction of the indirect effect, Q. J. Roy. Meteor. Soc., 134, 1143– 1154, 2008.

Hintze, J. L. and Nelson, R. D.: Violin Plots: A Box Plot-Density Trace Synergism, Am. Stat., 52(2), 181–184, 1998.

540 Johnson, B. T., Shine, K. P., and Forster, P. M.: The semi-direct aerosol effect: Impact of absorbing aerosols on marine
stratocumulus, Q. J. R. Meteorol. Soc., 130, 1407–1422, 2004.

Johnson, B. T. T., Turnbull, K. F., Brown, P. R., Burgess, R., Dorsey, J. R., Baran, A. J., Webster, H. N., Haywood, J. M.,
Cotton, R., Ulanowski, J., Hesse, E., Woolley, A. M., and Rosenberg, P.: Insitu observations of volcanic ash clouds
from the FAAM aircraft during the eruption of Eyjafjallajokull in 2010, J. Geophys. Res., ¨ 117, D00U24,
545   doi:10.1029/2011JD016760, 2012.

Keil, A. and Haywood, J. M.: Solar radiative forcing by biomass burning aerosol particles during SAFARI 2000: A case
study based on measured aerosol and cloud properties, J. Geophys. Res. Atmos., 108(D13), doi:10.1029/2002JD002315,
2003.

King, W. D., Parkin, D. A., and Handsworth, R. J.: A hot-wire liquid water device having fully calculable response
550   characteristics, J. Appl. Meteor., 1809–1813, 1978.

Klein, S. A. and Hartmann, D. L.: The seasonal cycle of low stratiform clouds, J. Climate, 6, 1587–1606, 1993.

Korolev, A.: Reconstruction of the sizes of spherical particles from their shadow images. Part I: Theoretical considerations,
J. Atmos. Ocean. Tech., 24, 376–389, 2007.

Kuo, H. and Schubert, W.: Stability of cloud-topped boundary layers, Q. J. Roy. Meteorol. Soc., 114, 887–916, 1988.

555 Lance, S., Brock, C. A., Rogers, D., and Gordon, J. A.: Water droplet calibration of the Cloud Droplet Probe (CDP) and
inflight performance in liquid, ice and mixed-phase clouds during ARCPAC, Atmos. Meas. Tech., 3, 1683–1706,
doi:10.5194/amt3-1683-2010, 2010.

Lawson, R. P., Stewart, R. E., and Angus, L. J. : Observations and numerical simulations of the origin and development of
very large snowflakes, J. Atmos. Sci., 55, 3209–3229, 1998.

560 Lawson, R. P., O'Connor, D., Zmarzly, P., Weaver, K., Baker, B. A., Mo, Q., and Jonsson, H.: The 2D-S (Stereo) probe:
Design and preliminary tests of a new airborne, high-speed, high-resolution imaging probe, J. Atmos. Ocean. Tech., 23,
1462–1477, 2006.

Atmospheric
Chemistry
and Physics
Discussions

LeBlanc, S. E., Redemann, J., Flynn, C., Pistone, K., Kacenelenbogen, M., Segal-rosenheimer, M., Shinozuka, Y., Dunagan, S., Dahlgren, R. P., Meyer, K., Podolske, J., Howell, S. G., Freitag, S., Small-griswold, J., Holben, B., Diamond, M., Wood, R., Formenti, P., Piketh, S., Maggs-Kölling, G., Gerber, M. and Namwoonde, A.: Above-cloud aerosol optical depth from airborne observations in the southeast Atlantic, Atmos. Chem. Phys., 20, 1565–1590, doi:10.5194/acp-20-1565-2020, 2020.

Lock, A. P.: Factors influencing cloud area at the capping inversion for shallow cumulus clouds, Q. J. Roy. Meteorol. Soc., 135, 941– 952, 2009.

McFarquhar, G. M. and Wang, H.: Effects of Aerosols on Trade Wind Cumuli over the Indian Ocean: Model Simulations, Q. J. R. Meteorol. Soc., 132, 821–843, 2006.

McFarquhar, G. M., Zhang, G., Poellot, M. R., Kok, G. L., McCoy, R., Tooman, T., Fridlind, A., and Heymsfield, A. J.: Ice properties of single-layer stratocumulus during the Mixed-Phase Arctic Cloud Experiment: 1. Observations, J. Geophys. Res., 112, D24201, doi:10.1029/2007jd008633, 2007.

McFarquhar, G. M., Baumgardner, D., Bansemer, A., Abel, S. J., Crosier, J., French, J., Rosenberg, P., Korolev, A., Schwarzoenboeck, A., Leroy, D., Um, J., Wu, W., Heymsfield, A. J., Twohy, C., Detwiler, A., Field, P., Neumann, A., Cotton, R., Axisa, D., Dong, J., McFarquhar, G. M., Baumgardner, D., Bansemer, A., Abel, S. J., Crosier, J., French, J., Rosenberg, P., Korolev, A., Schwarzoenboeck, A., Leroy, D., Um, J., Wu, W., Heymsfield, A. J., Twohy, C., Detwiler, A., Field, P., Neumann, A., Cotton, R., Axisa, D., and Dong, J.: Processing of Ice Cloud In Situ Data Collected by Bulk Water, Scattering, and Imaging Probes: Fundamentals, Uncertainties, and Efforts toward Consistency, Meteorol. Monogr., 58, 11.1–11.33, https://doi.org/10.1175/AMSMONOGRAPHSD-16-0007.1, 2017.

McFarquhar, G. M., Finlon, J. A., Stechman, D. M., Wu, W., Jackson, R. C., and Freer, M.: University of Illinois/Oklahoma Optical Array Probe (OAP) Processing Software, https://doi.org/10.5281/zenodo.1285969, 2018.

Mellado, J. P.: Cloud-top entrainment in stratocumulus clouds, Ann. Rev. Fluid Mech., 49, 145–169, 2017.

Myhre, G., Shindell, D., Bréon, F.-M., Collins, W., Fuglestvedt, J., Huang, J., Koch, D., Lamarque, J.-F., Lee, D., Mendoza, B., Nakajima, T., Robock, A., Stephens, G., Takemura, T. and Zhang, H.: Anthropogenic and Natural Radiative Forcing. In: Climate Change 2013: The Physical Science Basis. Contribution of Working Group I to the Fifth Assessment Report of the Intergovernmental Panel on Climate Change, edited by: Stocker, T. F., Qin, D., Plattner, G.-K., Tignor, M., Allen, S. K., Boschung, J., Nauels, A., Xia, Y., Bex, V., and Midgley, P. M., Cambridge University Press, Cambridge, United Kingdom and New York, NY, USA, 571–657, 2013.

Oreopoulos, L. and Rossow, W. B.: The cloud radiative effects of International Satellite Cloud Climatology Project weather states, J. Geophys. Res.-Atmos., 116, D12202, doi:10.1029/2010JD015472, 2011.

Painemal, D. and Zuidema, P.: Assessment of MODIS cloud effective radius and optical thickness retrievals over the Southeast Pacific with VOCALS-REx in situ measurements, J. Geophys. Res., 116, D24206, doi:10.1029/2011jd016155, 2011.

Atmospheric
Chemistry
and Physics
Discussions

Painemal, D., Chang, F.-L., Ferrare, R., Burton, S., Li, Z., Smith Jr., W. L., Minnis, P., Feng, Y., and Clayton, M.: Reducing uncertainties in satellite estimates of aerosol–cloud interactions over the subtropical ocean by integrating vertically resolved aerosol observations, Atmos. Chem. Phys., 20, 7167–7177, https://doi.org/10.5194/acp-20-7167-2020, 2020.

Pawlowska, H. and Brenguier, J.-L.: An observational study of drizzle formation in stratocumulus clouds for general circulation model (GCM) parameterizations, J. Geophys. Res., 108, 8630, doi:10.1029/2002JD002679, 2003.

Pistone, K., Redemann, J., Doherty, S., Zuidema, P., Burton, S., Cairns, B., Cochrane, S., Ferrare, R., Flynn, C., Freitag, S., Howell, S. G., Kacenelenbogen, M., LeBlanc, S., Liu, X., Schmidt, K. S., Sedlacek III, A. J., Segal-Rozenhaimer, M., Shinozuka, Y., Stamnes, S., van Diedenhoven, B., Van Harten, G., and Xu, F.: Intercomparison of biomass burning aerosol optical properties from in situ and remote-sensing instruments in ORACLES-2016, Atmos. Chem. Phys., 19, 9181–9208, https://doi.org/10.5194/acp-19-9181-2019, 2019.

Redemann, J., et al.: An overview of the ORACLES (ObseRvations of Aerosols above CLouds and their intEractionS) project: aerosol-cloud-radiation interactions in the Southeast Atlantic basin, Atmos. Chem. Phys. Discuss., https://doi.org/10.5194/acp-2020-449, in review, 2020.

Roberts, G. C. and Nenes, A.: A continuous-flow streamwise thermal-gradient CCN chamber for atmospheric measurements, Aerosol Sci. Tech., 39, 206–221, doi:10.1080/027868290913988, 2005.

Rosenfeld, D., Andreae, M. O., Asmi, A., Chin, M., de Leeuw, G., Donovan, D., Kahn, R., Kinne, S., Kivekäs, N., Kulmala, M., Lau, W., Schmidt, S., Suni, T., Wagner, T., Wild, M., and Quaas, J.: Global observations of aerosol-cloud precipitation-climate interactions, Rev. Geophys., 52, 750–808, doi:10.1002/2013RG000441, 2014.

Small, J. D., Chuang, P. Y., Feingold, G., and Jiang, H.: Can aerosol decrease cloud lifetime?, Geophys. Res. Lett., 36, 16806, doi:10.1029/2009GL038888, 2009.

Sorooshian, A., Feingold, G., Lebsock, M. D., Jiang, H., and Stephens, G. L.: On the precipitation susceptibility of clouds to aerosol perturbations, Geophys. Res. Lett., 36, L13803, doi:10.1029/2009GL038993, 2009.

Stein, A. F., Draxler, R. R., Rolph, G. D., Stunder, B. J. B., Cohen, M. D., and Ngan, F.: NOAA's HYSPLIT Atmospheric Transport and Dispersion Modeling System, B. Am. Meteorol. Soc., 96, 2059–2077, doi:10.1175/BAMS-D-14-00110.1, 2015.

Stephens, M., Turner, N., and Sandberg, J.: Particle identification by laser-induced incandescence in a solid-state laser cavity. Appl. Opt. 42, 3726-3736, 2003.

Strapp, J. W., Leaitch, W. R., and Liu, P. S. K.: Hydrated and Dried Aerosol-Size-Distribution Measurements from the Particle Measuring Systems FSSP-300 Probe and the Deiced PCASP-100x Probe, J. Atmos. Oceanic Technol., 9, 548–555, 1992.

Thornhill, K. L., Anderson, B. E., Barrick, J. D. W., Bagwell, D. R., Friesen, R., and Lenschow, D.: Air motion inter-comparison flights during Transport and Chemical Evolution in the Pacific (TRACE-P)/ACE-ASIA, J. Geophys. Res., 108, https://doi.org/10.1029/2002JD003108, 2003.

Twomey, S.: Pollution and the Planetary Albedo, Atmos. Environ., 8, 1251–1256, 1974.

630 Twomey, S.: The influence of pollution on the shortwave albedo of clouds. J. Atmos. Sci., 34, 1149-1152, 1977.

Warren, S. G., Hahn, C. J., London, J., Chervin, R. M., and Jenne, R. L.: Global Distribution of Total Cloud Cover and Cloud type Amounts Over the Ocean, NCAR Technical Note NCAR/TN317+STR, 1988.

Wang, Y., McFarquhar, G.M., Rauber, R.M., Zhao, C., Wu, W., Finlon, J.A., Stechman, D.M., Stith, J., Jensen, J.B., Schnaiter, M., Järvinen, E., Waitz, F., Vivekanandan, J., Dixon, M., Rainwater, B., and Toohey, D.W.: Microphysical
635   properties of generating cells over the Southern Ocean: Results from SOCRATES. J. Geophys.Res., 125, e2019JD032237. https://doi.org/10.1029/2019JD032237, 2020.

Wood, R.: Stratocumulus Clouds, Mon. Weather Rev., 140, 2373–2423, doi:10.1175/MWR-D-11-00121.1, 2012.

Yamaguchi, T., Feingold, G., Kazil, J., and McComiskey, A.: Stratocumulus to cumulus transition in the presence of elevated smoke layers, Geophys. Res. Lett., 42, 10478–10485, https://doi.org/10.1002/2015GL066544, 2015.

640 Zuidema, P., Redemann, J., Haywood, J., Wood, R., Piketh, S., Hipondoka, M. and Formenti, P.: Smoke and Clouds above the Southeast Atlantic: Upcoming Field Campaigns Probe Absorbing Aerosol's Impact on Climate, Bull. Am. Meteorol. Soc., 160129100143006, doi:10.1175/BAMS-D-15-00082.1, 2016.

645

650

655

660

Atmospheric
Chemistry
and Physics
Discussions

665 **Table 1: Primary measurement, sampling frequency and measurement range of the in-situ instruments installed on the P-3 research aircraft.**

Instrument	Primary Measurement	Sampling Frequency	Measurement Range	Reference
Rosemount 102	Temperature	2 Hz	-50° to 50°C	Rosemount, Incorporated
Rosemount MADT 2014	Pressure	64 Hz	30 - 1300 mb	Rosemount, Incorporated
EdgeTech 137 Chilled-Mirror Hygrometer	Dew Point Temperature	0.5 Hz	-40° to 60°C	EdgeTech Instruments
Global Positioning System (GPS)	Latitude, Longitude, Altitude	1 Hz	-90 to 90° -180 to 180°	
Turbulent Air Motion Measurement System (TAMMS)	3-D wind components (u, v, w)	20 Hz	$0.05 - 410$ m s^{-1}	Thornhill et al. (2003)
CO/CO2/H2O Analyzer	CO, H_2O (v)	1 Hz	5 to 50,000 ppb, 100 ppm to 100% humidity	Los Gatos Research
Cloud and Aerosol Spectrometer (CAS)	Droplet n(D)	10 Hz	0.5 - 50 µm	Baumgardner et al. (2001)
Cloud Droplet Probe (CDP)	Droplet n(D)	10 Hz	2 - 50 µm	Lance et al. (2010)
Phase Doppler Interferometer (PDI)	Droplet n(D)	1 Hz	3 - 1,500 µm	Chuang et al. (2008)
2D-Stereo Probe (2-DS)	Droplet Images, asynchronous n(D)		Nominally 10 - 1,280 µm	Lawson et al. (2006)
Cloud Imaging Probe (CIP)	Droplet Images, asynchronous n(D)		Nominally 25 - 1,600 µm	Baumgardner et al. (2001)
High Volume Precipitation Sampler (HVPS-3)	Droplet Images, asynchronous n(D)		Nominally 150 - 19,200 µm	Lawson et al. (1998)
King Hot-wire	Bulk LWC	25 Hz	$0.05 - 3$ g m^{-3}	King et al. (1978)
CAPS Hot-wire (LWC-100)	Bulk LWC	10 Hz	$0.05 - 3$ g m^{-3}	Baumgardner et al. (2001)
Ultra-High Sensitivity Aerosol Spectrometer (UHSAS)	Aerosol n(D)	1 Hz	0.06 - 1 µm	Cai et al. (2008)
Passive Cavity Aerosol Spectrometer Probe (PCASP)	Aerosol n(D)	10 Hz	0.1 - 3 µm	Strapp et al. (1992)
Single Particle Soot Photometer (SP2)	Aerosol Absorption	1 Hz	55 - 524 nm	Stephens et al. (2003)
Cloud Condensation Nuclei counter (CCN-100)	CCN concentration	1 Hz	0.1% - 0.4% supersaturation	Roberts and Nenes (2005)
High Resolution Time-of-Flight Aerosol Mass Spectrometer (HR-ToF-AMS)	Aerosol Mass	0.2 Hz	50 - 700 nm	Drewnick et al. (2005)

Atmospheric
Chemistry
and Physics
Discussions

Table 2: List of research flights analyzed with the number of cloud profiles flown and total time spent profiling clouds during each flight. The number of profiles during sawtooth maneuvers is reported within parentheses. The number of profiles and the corresponding sampling time is reported for Contact and Separated profiles during each flight.

Flight Date	Sawtooth + individual profiles	Cloud time	Contact profiles	Separated profiles
PRF5: September 06	4 (4, 5, 4, 6) + 5	1327 s	13 (857 s)	11 (470 s)
PRF7: September 10	1 (2) + 7	461 s	0 (0 s)	9 (461 s)
PRF8: September 12	1 (6) + 2	504 s	1 (32 s)	7 (472 s)
PRF9: September 14	0 (0) + 8	574 s	0 (0 s)	8 (574 s)
PRF11: September 20	1 (7) + 6	669 s	13 (669 s)	0 (0 s)
PRF13: September 25	2 (2, 3) + 4	511 s	3 (148 s)	6 (363 s)
Total	9 (39) + 32	1h 7m 26s	30 (1706 s)	41 (2340 s)

670 **Table 3: The above- and below-cloud aerosol and trace gas concentrations with the above-cloud Aerosol Optical Depth (AOD) for four sawtooth maneuvers (S1-S4) flown on 6 September 2016. The values correspond to averages across the individual profiles flown during each sawtooth maneuver.**

Sawtooth/ Parameter	S1	S2	S3	S4
Above-cloud total M_a $(OA + SO_4^{2+} + NH_4^+ + NO_3^-)$	3.4	23	22	0.8
Below-cloud	4.5	5.9	5.7	1.4
Above-cloud OA M_a ($\mu g\ m^{-3}$)	2	16	13	0.5
Below-cloud	2	3	3	0.8
Above-cloud N_a (cm^{-3})	241	1515	1334	16
Below-cloud	354	327	390	72
Above-cloud rBC (cm^{-3})	66	516	700	10
Below-cloud	72	111	130	---
Above-cloud CO (ppb)	95	196	230	96
Below-cloud	93	103	117	88
Above-cloud AOD	0.33	0.37	0.49	0.39

675

680

Atmospheric
Chemistry
and Physics
Discussions

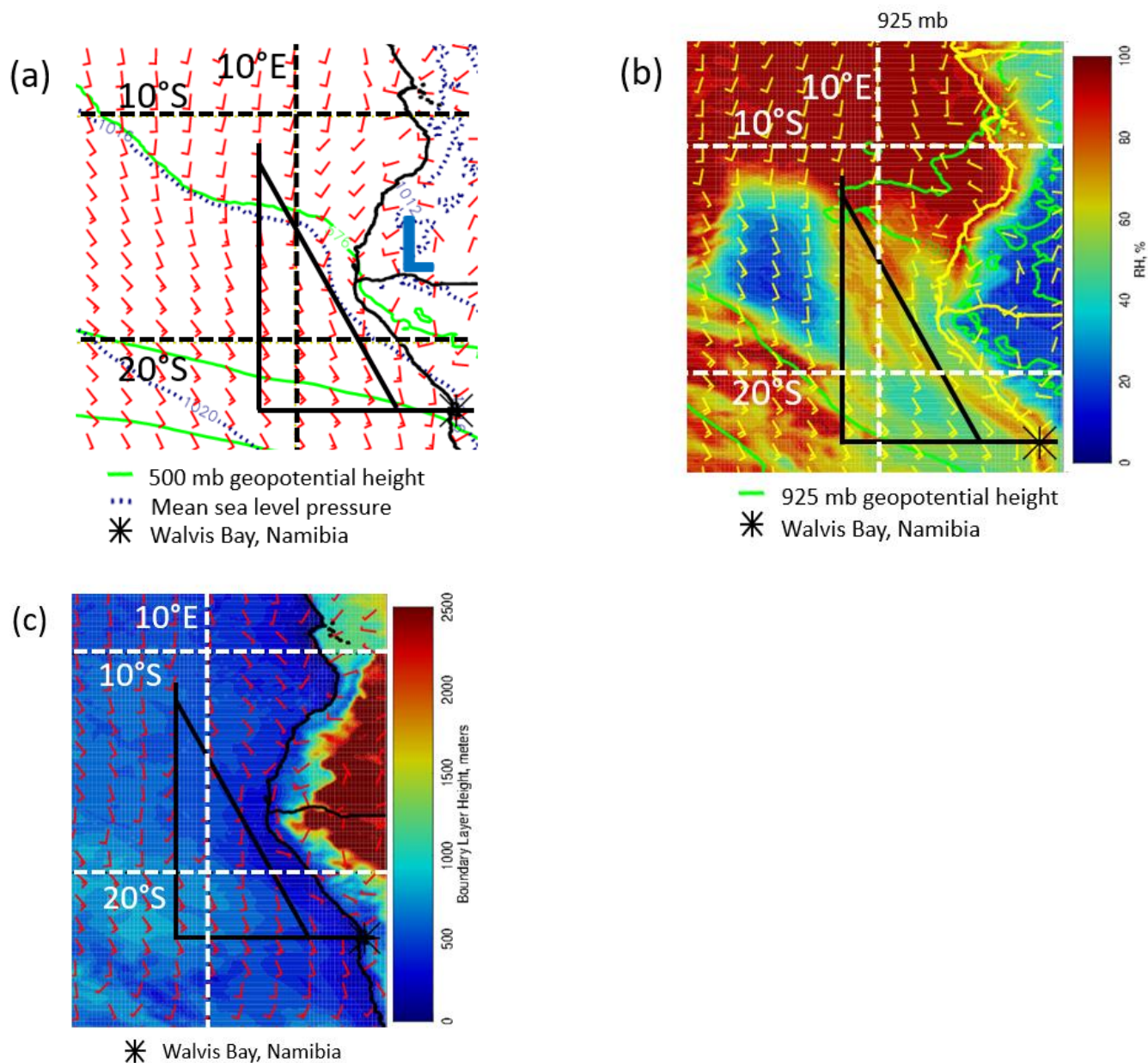**Table 4: The range of time, latitude, longitude, above-cloud AOD and cloud top height (Z_T) for cloud profiles flown during the six flights. The lowest altitude where above-cloud $N_a > 500$ cm^{-3} was sampled during the flight (Z_{500}) is in the far-right column.**

Date	Time (UTC)	Latitude (°S)	Longitude (°E)	AOD	Z_T (m)	Z_{500} (m)
September 6	08:46 - 12:35	10.2 - 19.7	9.0 - 11.9	0.27 - 0.49	359 - 1002	680
September 10	09:09 - 12:36	14.1 - 18.7	4.0 - 8.6	0.21 - 0.29	990 - 1201	1800
September 12	11:16 - 12:26	9.7 - 12.9	-0.3 - 3.0	0.25 - 0.29	1146 - 1226	1200
September 14	09:36 - 14:16	16.4 - 18.1	7.5 - 9.0	0.31 - 0.32	635 - 824	2350
September 20	08:44 - 13:11	15.7 - 17.3	8.9 - 10.5	0.42 - 0.56	432 - 636	600
September 25	10:59 - 13:51	10.9 - 14.3	0.8 - 4.3	0.27 - 0.38	729 - 1124	1170

685 **Table 5: Differences between the average below- and above-cloud N_a, and the average N_c and R_e measured in the cloud layer for *contact* profiles relative to *separated* profiles. The differences are classified by the maximum below-cloud N_a within the boundary layer and correspond to 95% confidence intervals based on a two-sample t-test (not reported when $p > 0.05$).**

Maximum below-cloud N_a (cm^{-3})	Below-cloud N_a (cm^{-3})	Above-cloud N_a (cm^{-3})	N_c (cm^{-3})	R_e (μm)
Low N_a (< 300 cm^{-3})	-1.3 - -26.5	498.0 - 565.5	---	-0.1 - -0.6
High N_a (> 300 cm^{-3})	48.3 - 78.2	746.7 - 884.3	80.8 - 92.8	-1.1 - -1.3
Low N_a (< 350 cm^{-3})	---	592.7 - 669.4	22.8 - 34.9	-0.3 - -0.9
High N_a (> 350 cm^{-3})	39.1 - 70.5	737.8 - 884.4	75.5 - 88.4	-1.2 - -1.6

Atmospheric
Chemistry
and Physics
Discussions

Figure 1: Visible image from the Spinning Enhanced Visible and Infrared Imager at 14:00 UTC on 6 September 2016 (PRF5), overlaid by the PRF5 flight track, and colored by flight altitude. Circles indicate sawtooth maneuver (S) and individual cloud profile (P) locations.

690

Figure 2: 0-hour European Centre for Medium-Range Weather Forecasts reanalysis at 12:00 UTC on 6 September 2016 for (a) mean sea level pressure, 500mb geopotential height and surface wind, (b) 925mb relative humidity, geopotential height and wind, and (c) BL height and 900 mb wind.
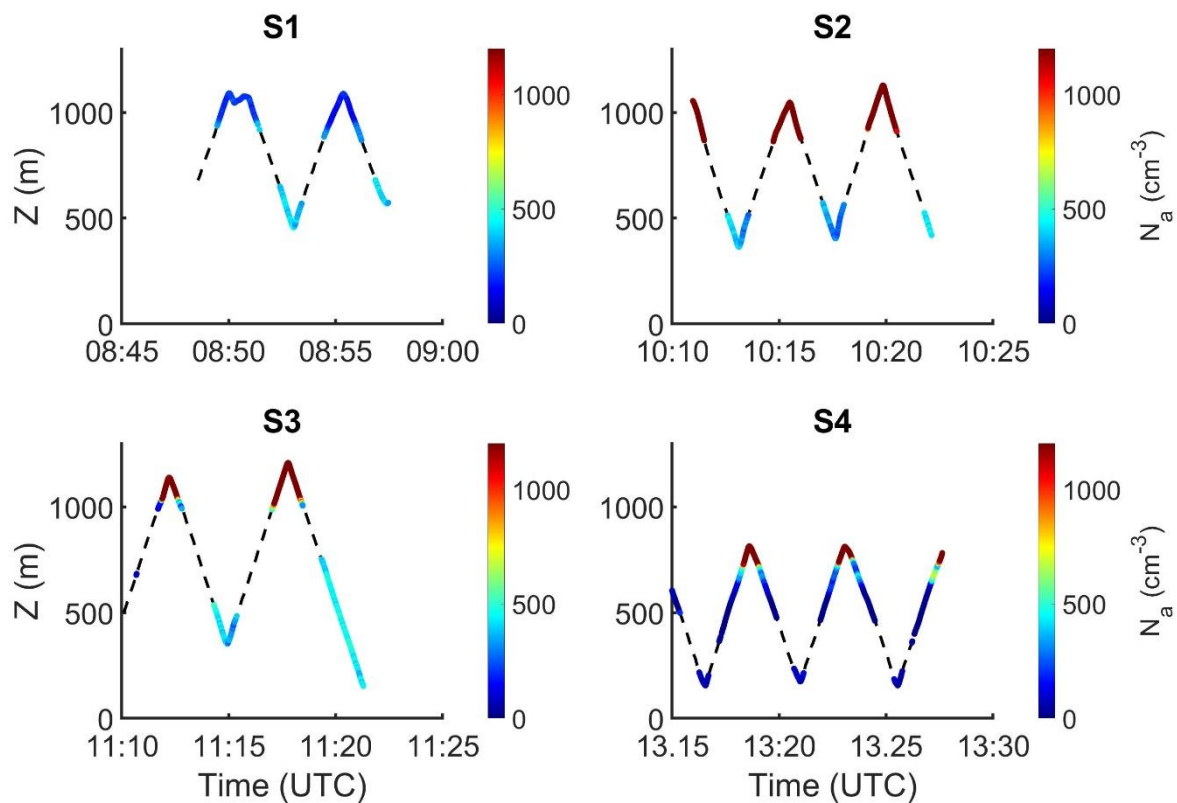
Figure 3: P-3 aircraft altitude as a function of time, colored by PCASP accumulation-mode (0.1 < D < 3 μm) N_a for 4 sawtooth
700 **maneuvers flown on 6 September 2016. Dashed lines indicate the cloud altitudes and in-cloud N_a are masked due to potential for droplet shattering on the PCASP probe inlet.**
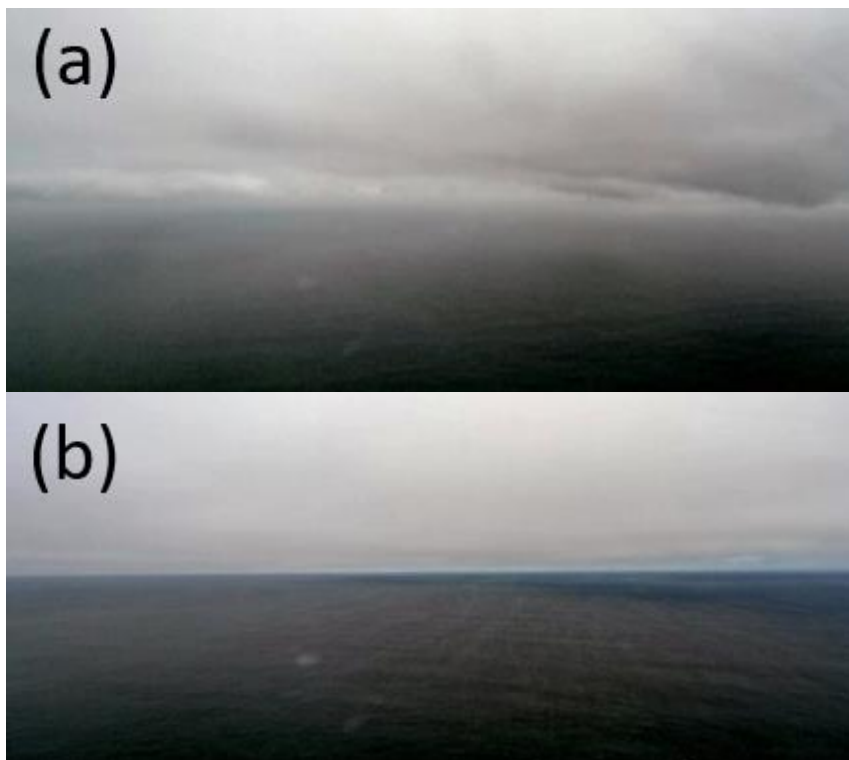
705 **Figure 4: Snapshots of the BL sampled below (a) S1 showing shallow cumulus and stratocumulus layers with varying bases, and (b) S4 showing stratocumulus clouds with a uniform base (NSRC/NASA Airborne Science Program)**
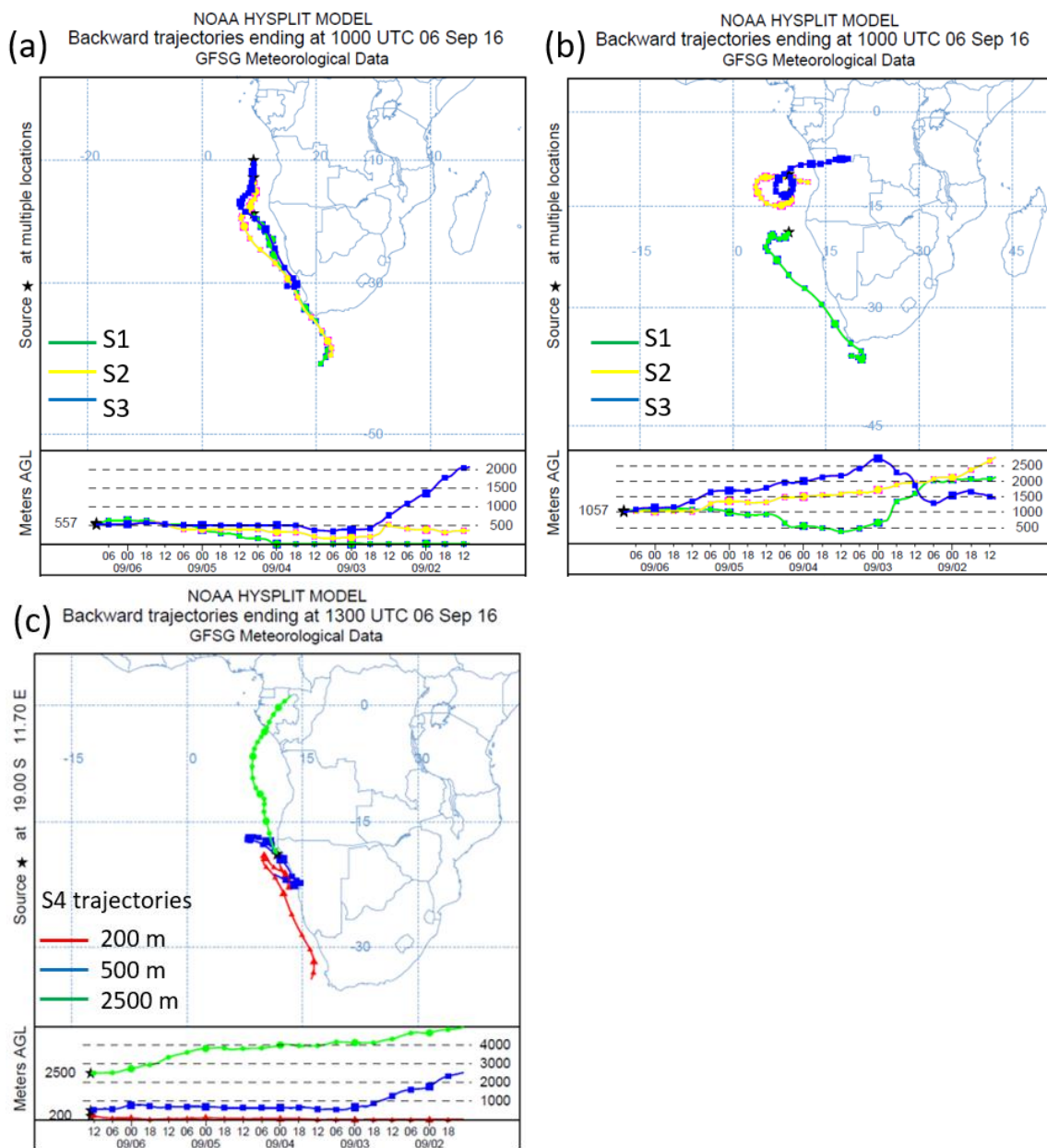
Figure 5: 5-day back-trajectories from the Hybrid Single Particle Lagrangian Integrated Trajectory model for sawtooth maneuvers flown on 6 September 2016 (a) ending at 10:00 UTC for S1-S3 at 500 m, (b) ending at 10:00 UTC for S1-S3 at 1000 m and (c) ending at 13:00 UTC for S4 at 200 m, 500 m and 2500 m (altitudes represent values above mean sea level)
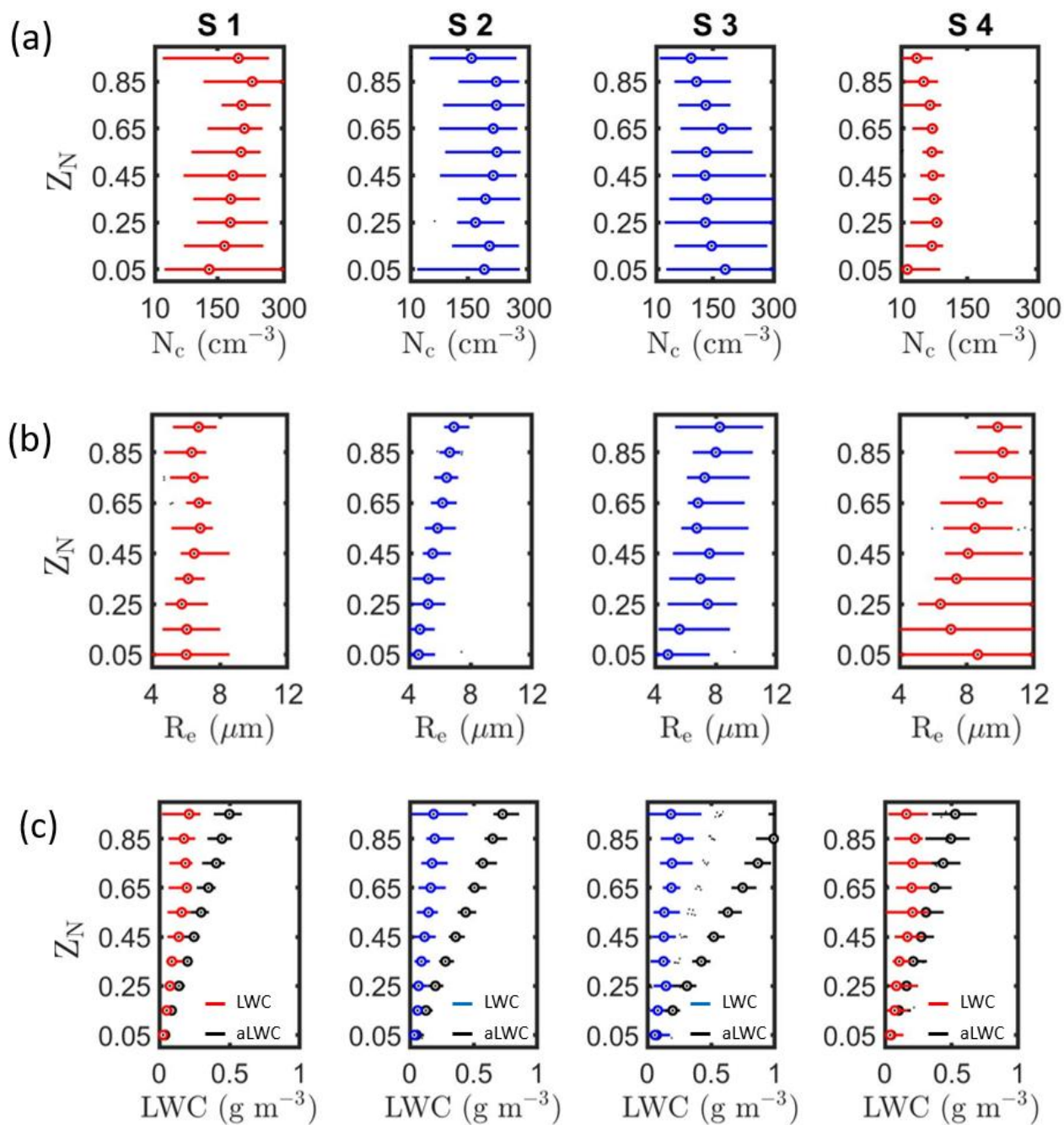
Figure 6: Vertical profiles of (a) N_c, (b) R_e and (c) LWC and aLWC as a function of Z_N for the 4 sawtooth maneuvers. Maneuvers
720 **with contact (separation) between the biomass-burning aerosol layer and cloud tops shown in blue (red).**
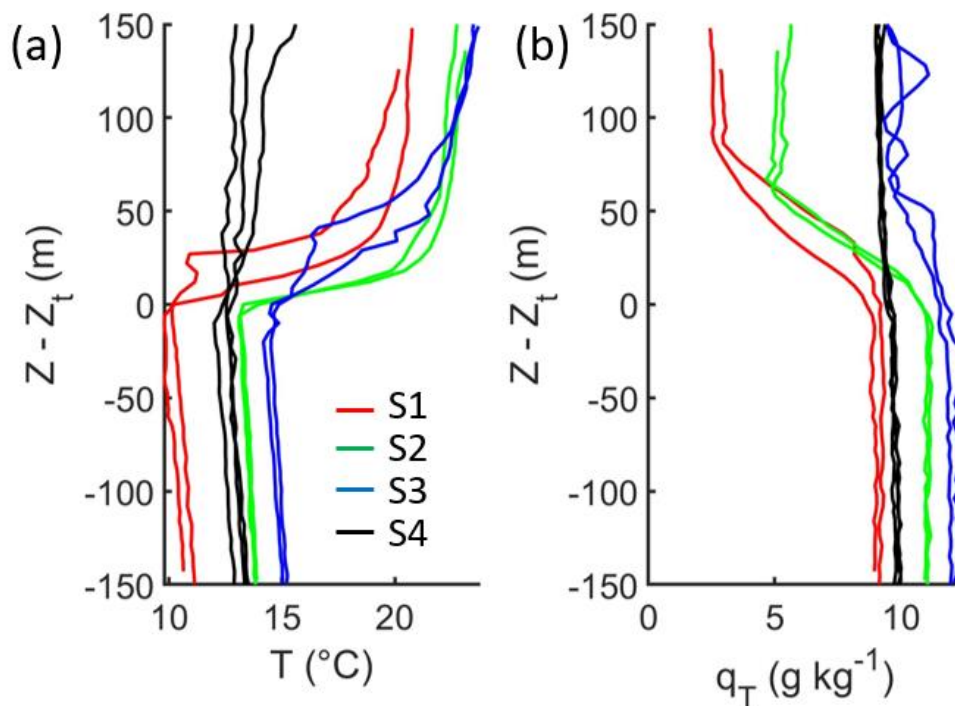
Figure 7: Vertical profiles of (a) T and (b) q_T as a function of distance from cloud top. Each line corresponds to an individual ascent through cloud during a sawtooth. The profiles flown during S2 and S3 (S1 and S4) had contact (separation) between the above-cloud biomass-burning aerosol layer and cloud tops.
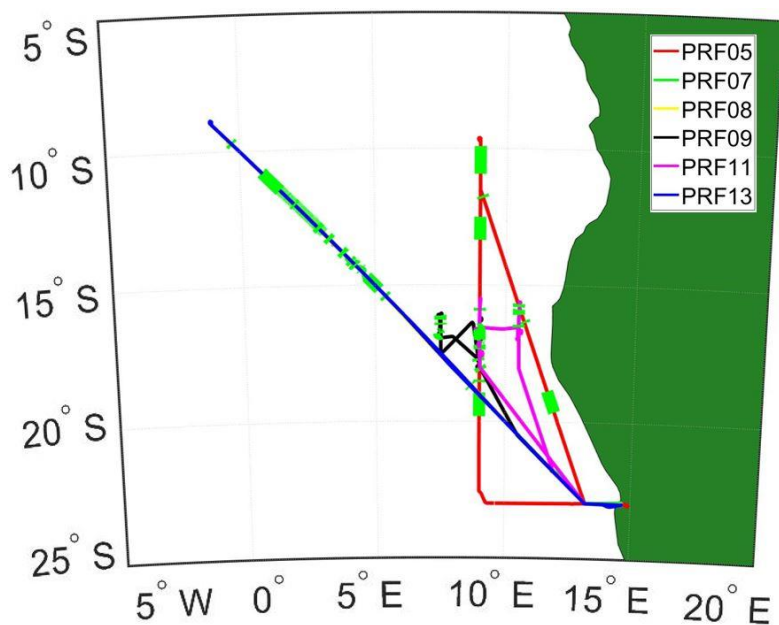

Figure 8: Flight tracks from PRFs 5, 7, 8, 9, 11 and 12 flown on 6, 10, 12, 14, 20 and 25 September 2016 with green segments indicating location of cloud profiles (flight tracks from PRFs 7 and 8 coincide with PRF13 and hence are not visible).
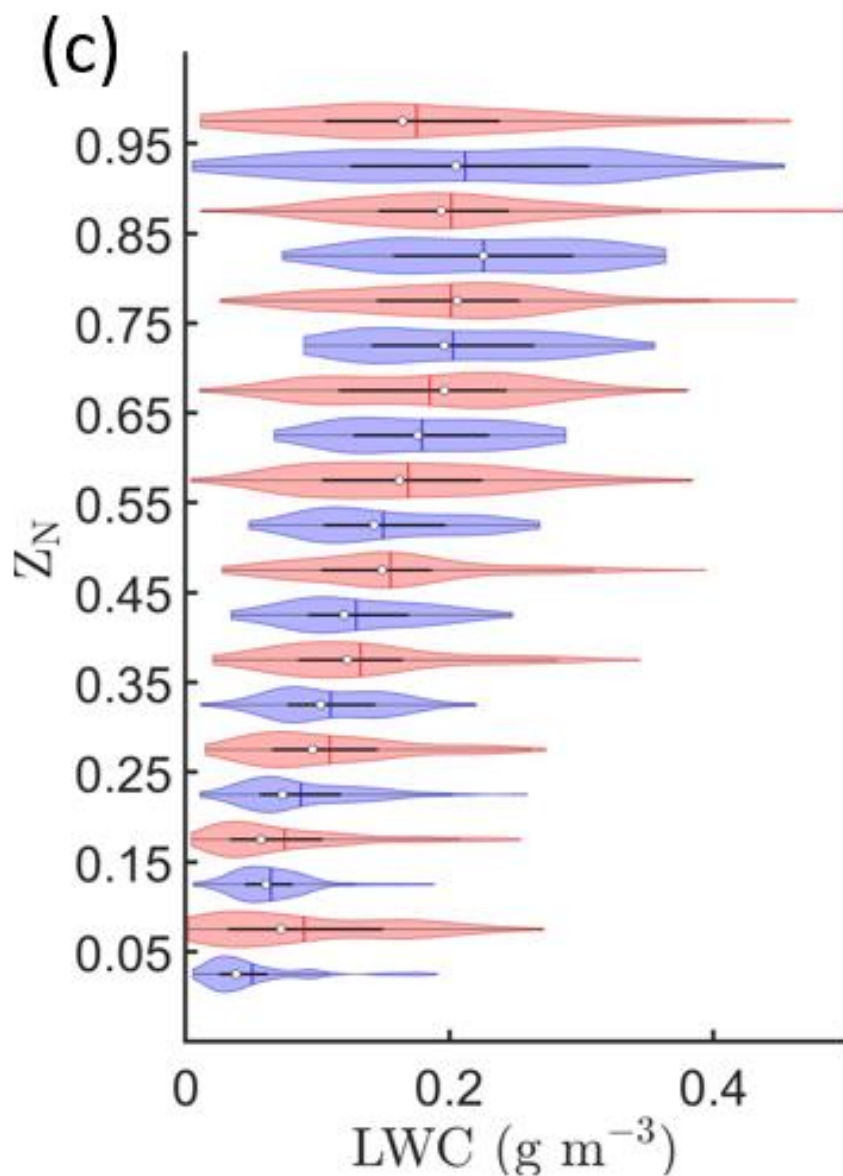
725
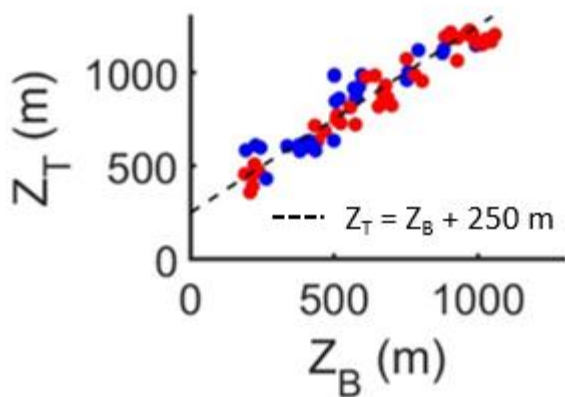
730

Figure 9: Cloud base and top heights for contact (blue) and separated (red) profiles flown during the six PRFs.

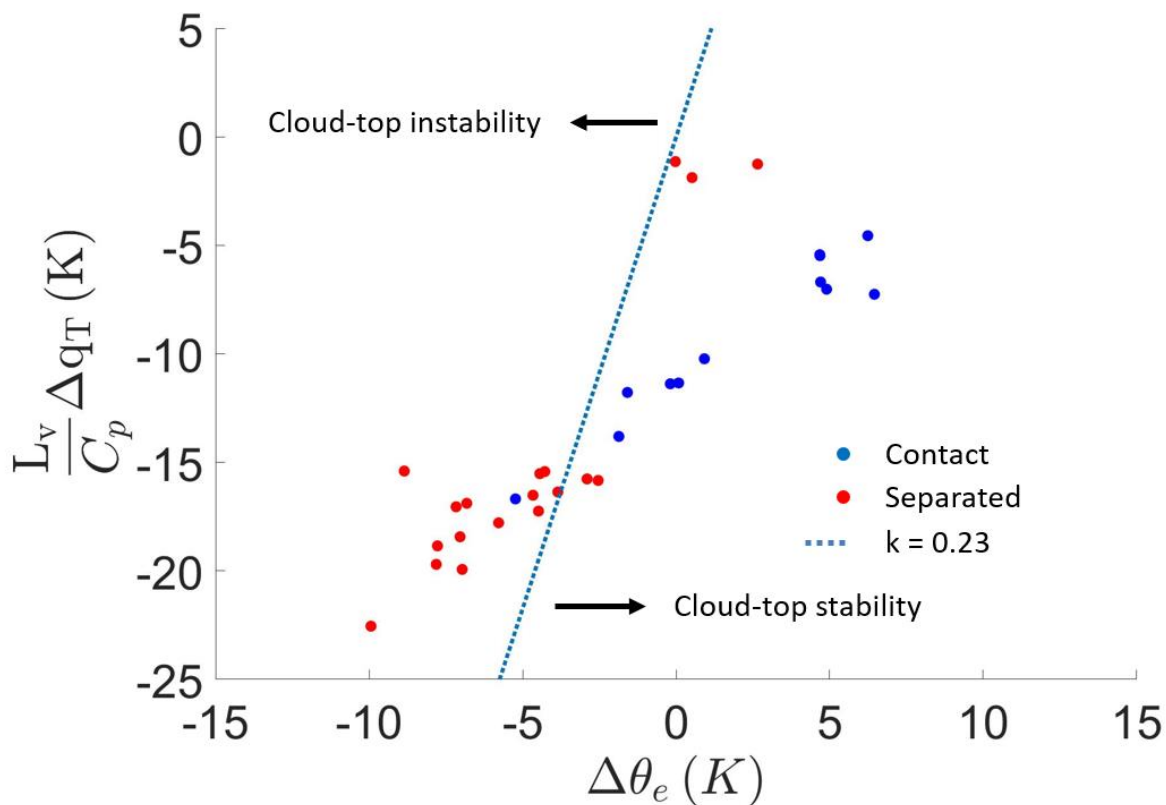Atmospheric
Chemistry
and Physics
Discussions
Open Access
EGU
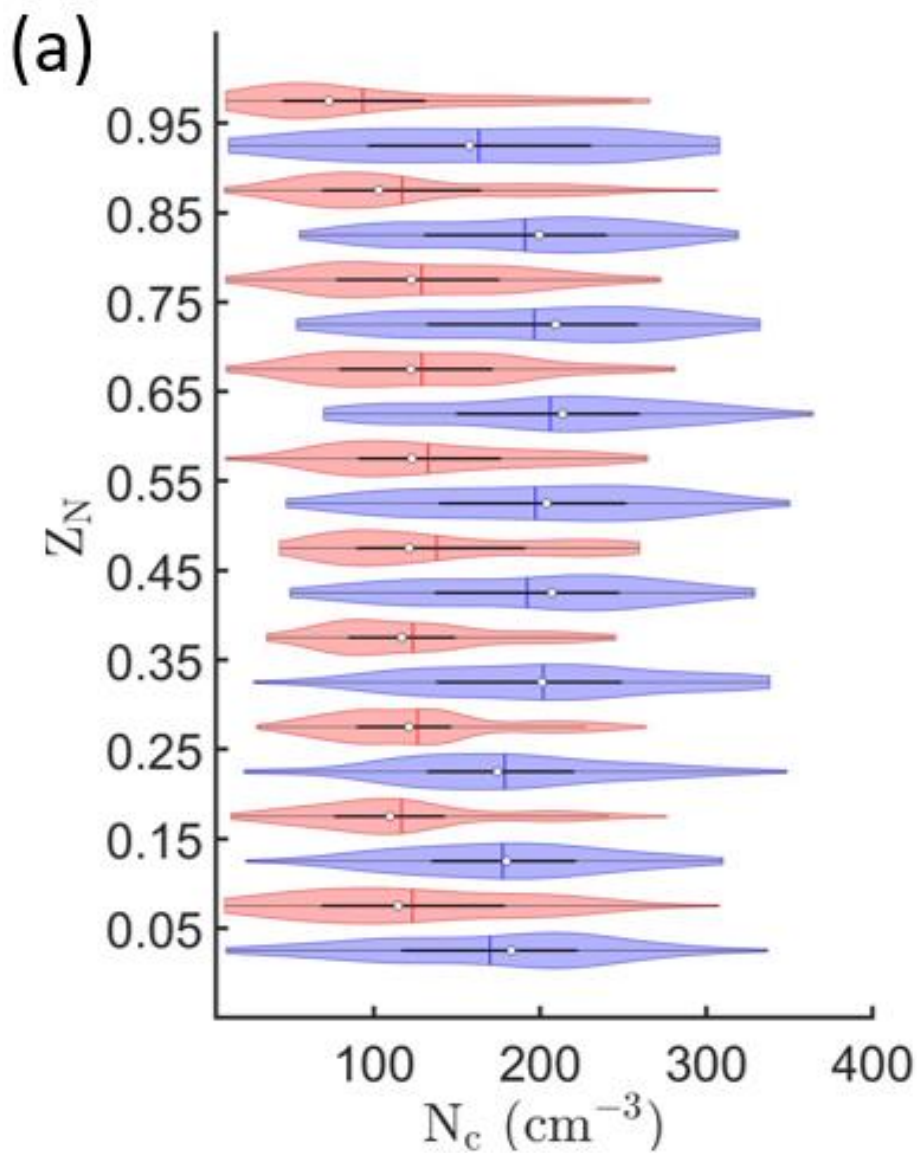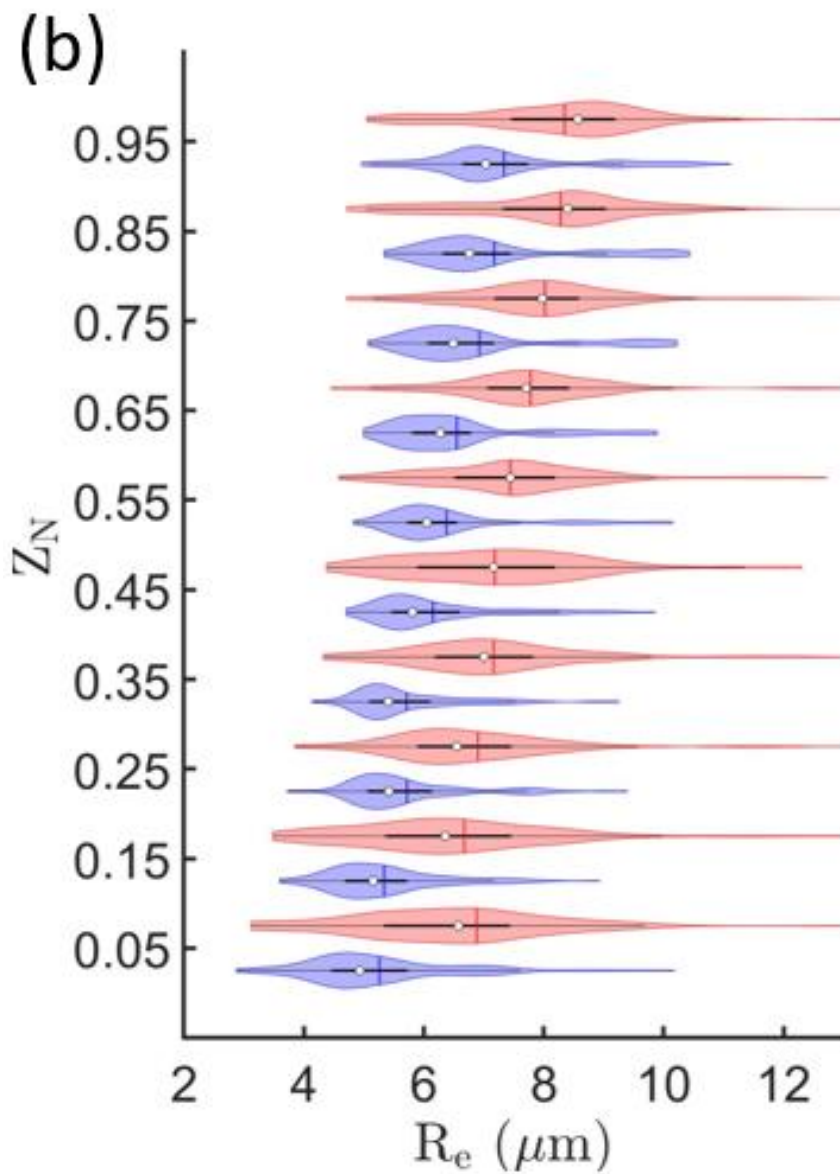
735

Figure 10: Kernel density estimates (indicated by the width of shaded area) and boxplots showing the 25th (Q1), 50th (white point) and 75th (Q3) percentile for (a) N_c (b) R_e and (c) LWC as a function of Z_N for contact (blue) and separated (red) profiles.

Atmospheric
Chemistry
and Physics
Discussions
Open Access
EGU

Figure 11: Difference between equivalent potential temperature (θ_e) and total water mixing ratio (q_T) measured within cloud and 100 m above cloud top for contact (blue) and separated (red) profiles (only ascents through cloud shown).
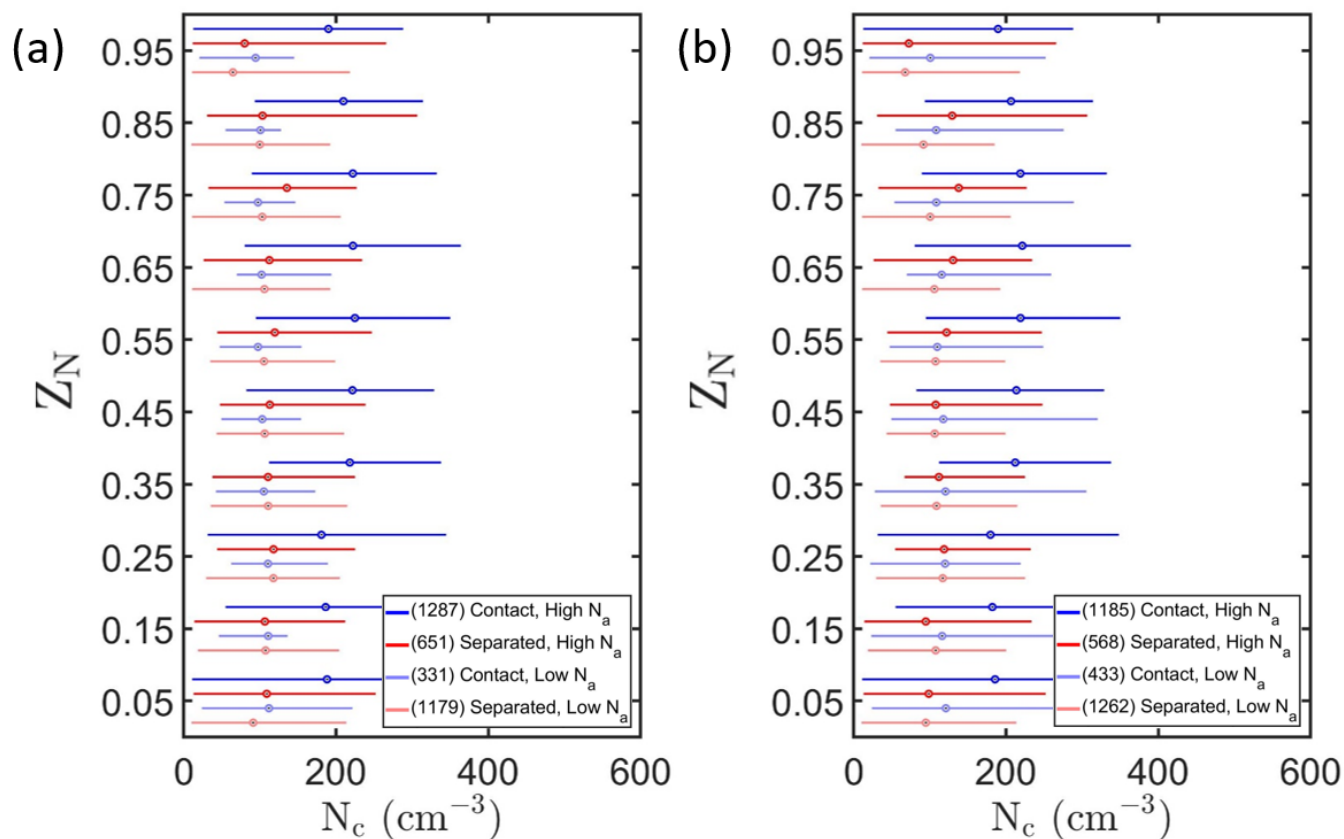
Figure 12: Boxplots representing N_c as a function of Z_N for contact (blue) and separated (red) profiles within boundary layers with high-N_a (darker) or low-N_a (lighter). The number of 1 Hz measurements within each regime is listed within parentheses. A high-N_a boundary layer is defined as having maximum N_a up to 100 m below cloud base (a) greater than 300 cm^{-3} and (b) greater than 350 cm^{-3}.